

**DTIC FILE COPY**

4

TECHNICAL REPORT BRL-TR-2960

**BRL**

1938 - Serving the Army for Fifty Years - 1988

AD-A202 411

**TRANSONIC NAVIER-STOKES COMPUTATIONS FOR A  
PROJECTILE AT ANGLE OF ATTACK AND  
COMPARISON WITH EXPERIMENT**

**CHING-CHANG CHIENG (NRC)  
JAMES E. DANBERG**

DECEMBER 1988

**DTIC  
ELECTE  
JAN 12 1989  
S H D**

APPROVED FOR PUBLIC RELEASE; DISTRIBUTION UNLIMITED.

U.S. ARMY LABORATORY COMMAND

**BALLISTIC RESEARCH LABORATORY  
ABERDEEN PROVING GROUND, MARYLAND**

89 1 12 019

DESTRUCTION NOTICE

Destroy this report when it is no longer needed. DO NOT return it to the originator.

Additional copies of this report may be obtained from the National Technical Information Service, U.S. Department of Commerce, Springfield, VA 22161.

The findings of this report are not to be construed as an official Department of the Army position, unless so designated by other authorized documents.

The use of trade names or manufacturers' names in this report does not constitute indorsement of any commercial product.

REPORT DOCUMENTATION PAGE

1a. REPORT SECURITY CLASSIFICATION UNCLASSIFIED		1b. RESTRICTIVE MARKINGS	
2a. SECURITY CLASSIFICATION AUTHORITY		3. DISTRIBUTION / AVAILABILITY OF REPORT Approved for public release, distribution unlimited.	
2b. DECLASSIFICATION / DOWNGRADING SCHEDULE		5. MONITORING ORGANIZATION REPORT NUMBER(S)	
4. PERFORMING ORGANIZATION REPORT NUMBER(S) BRL-TR-2960		7a. NAME OF MONITORING ORGANIZATION	
6a. NAME OF PERFORMING ORGANIZATION U.S. Army Ballistic Research Laboratory	6b. OFFICE SYMBOL (if applicable) SLCBL-1F	7b. ADDRESS (City, State, and ZIP Code)	
6c. ADDRESS (City, State, and ZIP Code) Aberdeen Proving Ground, Maryland 21005-5066		9. PROCUREMENT INSTRUMENT IDENTIFICATION NUMBER	
8a. NAME OF FUNDING / SPONSORING ORGANIZATION	8b. OFFICE SYMBOL (if applicable)	10. SOURCE OF FUNDING NUMBERS	
8c. ADDRESS (City, State, and ZIP Code)		PROGRAM ELEMENT NO. 62618A	PROJECT NO. 11162618AHRD
		TASK NO. 00	WORK UNIT ACCESSION NO. 001 AJ
11. TITLE (Include Security Classification) Transonic Navier-Stokes Computations for a Projectile at Angle of Attack and Comparison with Experiment			
12. PERSONAL AUTHOR(S) CHING CHANG CHIENG* and JAMES F. DANBERG			
13a. TYPE OF REPORT Technical Report	13b. TIME COVERED FROM TO	14. DATE OF REPORT (Year, Month, Day)	15. PAGE COUNT
16. SUPPLEMENTARY NOTATION *National Tsing Hau University, Department of Nuclear Engineering, 855 Kuang Fu Road, Hsinchu, Taiwan 300, R. O. C.			
17. COSATI CODES		18. SUBJECT TERMS (Continue on reverse if necessary and identify by block number)	
FIELD	GROUP	Transonic Flow; Viscous Flow (code) Computation	
01	01	Wind Tunnel Experiment; Navier-Stokes	
19	0A		
19. ABSTRACT (Continue on reverse if necessary and identify by block number) The objective of this work is to investigate the ability of the Pulliam and Steger implicit Navier-Stokes code to predict the transonic, viscous flow about a body of revolution at small angles of attack. The computations have been performed for the geometry and test conditions of wind tunnel experiments. This includes surface pressure distributions and boundary layer surveys at Mach numbers of 0.94 and 0.97 and at 0 and 4 degrees angle of attack. Particular attention is focused on the boattail afterbody region because of the strong shock wave-boundary layer interactions and near wake influences which occur there. The results show good quantitative agreement between prediction and experiment for both pressure distribution and boundary layer profiles at zero angle of attack. To accurately predict the boattail characteristics in the final 2-3 percent of the body length, it was found necessary to correctly model the base and near wake flow. At four degrees angle of attack, the agreement is only fair.			
20. DISTRIBUTION / AVAILABILITY OF ABSTRACT <input type="checkbox"/> UNCLASSIFIED/UNLIMITED <input type="checkbox"/> SAME AS RPT. <input type="checkbox"/> DTIC USERS		21. ABSTRACT SECURITY CLASSIFICATION UNCLASSIFIED	
22a. NAME OF RESPONSIBLE INDIVIDUAL James F. Danberg		22b. TELEPHONE (Include Area Code) (301) 270 1200	22c. OFFICE SYMBOL SLCBL-1F-6

# ACKNOWLEDGEMENT

The authors wish to express their thanks to Mr. C. Nietubicz, Dr. J. Sahu and to Ms. K. Heavey for many helpful technical discussions and assistance in the use of the VSYM3D Code and the Cray 2 operating system. Their help was essential in completing this project in the short period of a single year.



Accession For		
NTIS GPA&I	<input checked="" type="checkbox"/>	
DTIC TAB	<input type="checkbox"/>	
Unannounced	<input type="checkbox"/>	
Justification		
By		
Distribution/		
Availability Codes		
Avail and/or		
Dist Special		
A-1		

# TABLE OF CONTENTS

	Page
I. INTRODUCTION . . . . .	1
II. EXPERIMENT . . . . .	3
1. FACILITY . . . . .	3
2. MODEL . . . . .	3
3. INSTRUMENTATION . . . . .	3
4. DATA REDUCTION . . . . .	4
III. COMPUTATIONAL TECHNOLOGY . . . . .	5
1. COMPUTATIONAL GRIDS . . . . .	7
IV. EFFECT OF DIFFERENT GRIDS . . . . .	9
1. SURFACE PRESSURE COEFFICIENTS . . . . .	9
2. VELOCITY PROFILE . . . . .	10
3. MACH NUMBER CONTOURS . . . . .	10
V. COMPARISON OF NUMERICAL PREDICTION WITH EXPERIMENT .	11
1. PRESSURE COEFFICIENT DISTRIBUTION AT $\alpha = 0^\circ$ . . . . .	11
2. VELOCITY PROFILES AT $\alpha = 0^\circ$ . . . . .	11
3. EFFECT OF ANGLE OF ATTACK . . . . .	12
VI. CLOSING REMARKS . . . . .	13
REFERENCES . . . . .	43
LIST OF SYMBOLS . . . . .	47
APPENDIX . . . . .	49
1. DATA REDUCTION . . . . .	49
2. DATA TABLES . . . . .	50
DISTRIBUTION LIST . . . . .	67

## LIST OF FIGURES

Figure		Page
1	General arrangement of the NASA Langley Research Center transonic pressure tunnel. . . . .	15
2	Test section of the NASA Langley Research Center 8 foot transonic pressure tunnel. . . . .	16
3	Boattailed model configuration showing dimensions. . . . .	17
4	Boundary layer survey mechanism. . . . .	18
5	Flat base segmented grid. . . . .	19
6	Detail of flat base segmented grid near the base. . . . .	20
7	Wrapped around grid with flat base and sting. . . . .	21
8	Detail of wrapped around grid near the base. . . . .	22
9	Extended boattail grid. . . . .	23
10	Detail of extended boattail near the base. . . . .	24
11	Effect on $C_p$ of changing the number of normal grid points, $M_\infty=0.94$ , $\alpha = 0.0^\circ$ . . . . .	25
12	Comparison of surface pressure coefficient distribution for three base grid configurations, $M_\infty=0.94$ , $\alpha = 0.0^\circ$ . . . . .	26
13	Effect of grid refinement on surface pressure coefficient distribution for extended boattail grid, $M_\infty=0.94$ , $\alpha = 0.0^\circ$ . . . . .	27
14	Effect of the three base grids on the velocity profile at $X/L=0.989$ , $M_\infty=0.94$ , $\alpha = 0.0^\circ$ . . . . .	28
15	Mach number contours for the flat base grid without a sting. . . . .	29
16	Mach number contours for the wrapped around grid with a sting. . . . .	30
17	Mach number contours for the extended boattail grid. . . . .	31
18	Predicted pressure coefficient distributions and comparison with measurements, $M_\infty=0.97$ , $\alpha = 0.0^\circ$ . . . . .	32
19	Velocity profiles obtained with the wrapped around grid, $M_\infty=0.94$ , $\alpha = 0.0^\circ$ . . . . .	33
20	Comparison between predicted and measured velocity profiles using extended boattail grid, $M_\infty=0.97$ , $\alpha = 0.0^\circ$ . . . . .	34
21	Improved velocity profiles using wrapped around grid at $X/L=0.967$ and $0.989$ , $M_\infty=0.97$ , $\alpha = 0.0^\circ$ . . . . .	35

22	Mach number contours for Mach number 0.97 and $\alpha = 0.0^\circ$ . . . . .	36
23	Effect of angle of attack on $C_p$ and comparison with Danberg's data, $M_\infty=0.94$ , $\alpha = 4.0^\circ$ , 170x50x39 grid. . . . .	37
24	Effect of angle of attack on $C_p$ and comparison with Miller's data, $M_\infty=0.94$ , $\alpha = 4.0^\circ$ , 170x50x39 grid. . . . .	38
25	Afterbody velocity profiles at angle of attack using extended boattail grid, $M_\infty=0.94$ , $\alpha = 4.0^\circ$ . . . . .	39
26	Surface pressure coefficient distributions using wrapped around grid, $M_\infty=0.97$ , $\alpha = 4.0^\circ$ . . . . .	40
27	Velocity profiles using wrapped around grid, $M_\infty=0.97$ and $\alpha = 4.0^\circ$ . . . .	41

## LIST OF TABLES

Table		Page
1	Probe Radii. . . . .	4
2	Directory of Data Tables. . . . .	50
3	Pressure Coefficient Data at Zero Angle of Attack . . . . .	51
4	Surface Pressure Coefficient, $M_\infty = 0.94, \alpha = 4^\circ$ . . . . .	52
5	Surface Pressure Coefficient, $M_\infty = 0.97, \alpha = 4^\circ$ . . . . .	52
6	Velocity Data at Zero Angle of Attack for Mach Number 0.94 . . . . .	53
7	Velocity Data at Four Degrees Angle of Attack for Mach Number 0.94 . . . .	54
8	Velocity Data at Four Degrees Angle of Attack for Mach Number 0.94 . . . .	55
9	Velocity Data at Four Degrees Angle of Attack for Mach Number 0.94 . . . .	56
10	Velocity Data at Four Degrees Angle of Attack for Mach Number 0.94 . . . .	57
11	Velocity Data at Four Degrees Angle of Attack for Mach Number 0.94 . . . .	58
12	Velocity Data at Four Degrees Angle of Attack for Mach Number 0.94 . . . .	59
13	Velocity Data for Zero Angle of Attack for Mach Number 0.97 . . . . .	60
14	Velocity Data at Four Degrees Angle of Attack for Mach Number 0.97 . . . .	61
15	Velocity Data at Four Degrees Angle of Attack for Mach Number 0.97 . . . .	62
16	Velocity Data at Four Degrees Angle of Attack for Mach Number 0.97 . . . .	63
17	Velocity Data at Four Degrees Angle of Attack for Mach Number 0.97 . . . .	64
18	Velocity Data at Four Degrees Angle of Attack for Mach Number 0.97 . . . .	65

## I. INTRODUCTION

The primary objective of this work is to investigate the ability of a numerical computational technique to predict the transonic, viscous flow field around an axisymmetric projectile at zero and  $4^\circ$  angle of attack. The quality of the prediction is assessed by comparison with wind tunnel measurements including boundary layer surveys. Although the basic theory and algorithms needed for such computations have been available for 7 or 8 years, only recently have computer memory and speed improved to the point where three-dimensional, transonic, Navier-Stokes computations with adequate resolution are feasible. The results described here were performed on the BRL Cray 2 and Cray X-MP computers using a version of the Pulliam and Steger<sup>1</sup> implicit, finite difference code.

These computations correspond to the test conditions and the model configuration tested in the NASA Langley Transonic Pressure Tunnel in 1979-1980<sup>2</sup> but not previously reported in detail. Preliminary results from these tests were reported<sup>3</sup> in 1979, in which a limited comparison was made with a potential flow theory. The experiment involved measurements of the pressure distribution and boundary layer surveys on the afterbody of an artillery projectile based on a slightly modified version of the U.S. Army's M549. Since these measurements are restricted to the afterbody, the pressure distribution data over the entire identical body, obtained by Miller and Molnar,<sup>4</sup> is also used for comparison with the numerical results. Their experiment considered a number of other problem areas, such as: the effects of spin, large angle of attack ( $10^\circ$ ) and a rotating band protuberance. These topics are not considered here since the discussion is limited to a smooth, non-rotating body at a small angle of attack. Other transonic surface pressure distribution measurements on a similar, but not identical, shape have been obtained by Kayser<sup>5</sup> and Kayser and Whiton.<sup>6</sup>

Earlier efforts to compute the flowfields around axisymmetric bodies concentrated on applying small disturbance potential theory. For example, Krupp and Murman<sup>7</sup> successfully applied such an inviscid theory to airfoils and to several bodies of revolution at zero degrees angle of attack. Their results were in quite good agreement with the pressure measurements of McDivitt and Taylor<sup>8,9</sup> and Drougge.<sup>10</sup> Another full transonic potential flow analysis coupled with a three-dimensional integral boundary layer calculation was performed by Chow, et al.<sup>11</sup> They compared their predicted results with the experimental data of Shrewsbury<sup>12</sup> on boattailed afterbody, wind tunnel models at zero angle of attack. Reasonable agreement was cited at Mach number 0.8 but at 0.9 the discrepancies were considerably larger. Bailey<sup>13</sup> extended this approach to three-dimensions and the technique was applied to projectile like configurations by Reklis, et al.<sup>14</sup> Their calculations, however, were only applied to circular-arc data<sup>9</sup> and to ballistic range data on overall pitching moments. The ability of the theory to predict the pitching moments was not fully satisfactory, in that the estimated critical Mach number was significantly higher than indicated by the measurements. Stahara et al.<sup>15</sup> obtained better results using a modified form of the transonic equivalence rule. A composite solution was described by Reklis, et al.<sup>16</sup> in which the 3-D small disturbance potential theory provided the inviscid pressure distribution for a numerical three-dimensional boundary layer computation developed by Dwyer.<sup>17</sup> These results were compared to the data of Danberg.<sup>2</sup> The predicted surface pressures on the boattail were rather poorly estimated, although the three dimensional boundary layer re-

sults agreed with the measurements where the inviscid pressure distribution was correctly calculated.

Practical Navier-Stokes computations of transonic flows were significantly advanced through the development of the implicit, approximately factored method based on the work of Beam and Warming<sup>18</sup> and subsequently incorporated in the code of Pulliam and Steger.<sup>1</sup> The equations of motion, in this code, are written in generalized body oriented coordinates. The thin shear layer approximation is used to simplify the viscous terms and the resulting equations are linearized. Approximate factorization is carried out in formulation of the algorithm so that block inversion techniques can be used separately in the spatial coordinate directions. The Baldwin-Lomax algebraic turbulence model<sup>19</sup> was incorporated for high Reynolds number flows. This technique was applied, for the first time, to the transonic boattail afterbody flowfield by Deiwert.<sup>20</sup> He compared his results with the experimental data of Ruebush,<sup>21</sup> Benek,<sup>22</sup> and Shrewsbury<sup>12</sup> on afterbodies with plume simulators. He found that qualitative agreement between the computations and experiment was excellent but quantitatively there appeared to be areas where further study was needed.

Computations have also been made by Sahu and Danberg<sup>23</sup> using a more sophisticated turbulence model in which a two equation  $k-\epsilon$  model of Launder and Spalding<sup>24</sup> was used. This computation was compared to the  $\alpha = 0^\circ$  experimental results of Danberg<sup>2</sup> and the locally separated flow over an axisymmetric bump on which data had been obtained by Johnson et al.<sup>25</sup> Only a slight improvement in the flow computation was observed for attached flows using the  $k-\epsilon$  model as compared to the Baldwin-Lomax algebraic model although better results were obtained in the redevelopment region downstream of separation.

The Navier-Stokes technique was specialized to axisymmetric bodies with spin in the eta-invariant code<sup>26</sup> as well as generalized to three dimensions. These codes were applied by Nietubicz et al.<sup>26,27,28,29</sup> to projectiles and comparisons were made with the data of Danberg, and Kayser. Nietubicz<sup>29</sup> concluded that there was inadequate viscous resolution particularly for spinning bodies because of limitations in capacity of the computers (e.g., Cray 1S). Kayser and Whiton<sup>6</sup> also applied the inviscid code of Reklis and the early version of the Navier-Stokes codes to their data. They found that the inviscid codes did well on the forebody, fair on the cylindrical section but still rather poorly on the boattail.

The most recent results presented by Sahu and Nietubicz<sup>30</sup> and Sahu and Steger<sup>31</sup> overcome these objections by using the capacity of the Cray 2 and by using more advanced algorithms incorporating vector splitting and upwind differencing.<sup>32</sup> Improved grid resolution allowed Sahu<sup>33</sup> to obtain improved predictions of the  $0^\circ$  and  $4^\circ$  angle attack pressure distributions of Kayser and Whiton.

The current work is a continuation of these validation studies of the Pulliam and Steger technique but with the emphasis directed at evaluating current abilities to predict viscous effects at angle of attack using the grid resolution capabilities of the Cray 2.

## II. EXPERIMENT

As indicated previously, there are two wind tunnel experiments, which concern the same shape and size model, one by Danberg,<sup>2</sup> and the other by Miller and Molnar,<sup>4</sup> which will be used to evaluate the results computed here. The Miller and Molnar experiment is well documented in their report but the other experimental results are not generally available. Therefore the details of the experiment will be briefly discussed here.

### 1. FACILITY

The experiments, reported here, were performed in the NASA Langley Research Center 8 foot Transonic Pressure Tunnel (TPT). A general arrangement and sketch of the tunnel is shown in Figure 1. For the test of the boattail model, the tunnel was operated at one atmosphere supply pressure (101.3 kPa) and at a supply temperature of 322.2 K which resulted in a Reynolds number of  $13 \times 10^6$  per meter. The TPT is of slotted wall construction, as illustrated in Figure 2, to minimize reflected wave interference effects. The interference of the model, which introduced 0.69 per cent blockage of the tunnel flow, was monitored using tunnel wall static pressure taps. The model was sting mounted from the NASA support sector and roll mechanism which allowed measurements at angle of attack and in various roll positions.

The pressure distribution data reported here were obtained at tunnel Mach numbers of 0.94 and 0.97 and at 0 and 4 degrees angles of attack. Boundary layer surveys were made at six longitudinal stations near and on the boattail and at various orientations of the model.

### 2. MODEL

The tests were made using a U.S. Army Ballistic Research Laboratory model of a typical modern artillery projectile as illustrated in Figure 3. The configuration differed from the standard 155mm, M549 projectile in that the model was made 30 per cent larger (201.9mm diameter) to obtain better wind tunnel simulation of the flight Reynolds number. In addition, the rotating bands were omitted and the boattail was slightly modified in length and angle. The configuration consists of a blunted, secant-ogive nose followed by a cylindrical section and a 0.5 caliber, 7 degree conical boattail. Turbulent flow was assured by using a sand-grain roughness strip 5 cm from the blunted nose. The afterbody was instrumented with 14 static pressure orifices located so as to define the flow conditions in the vicinity of the boattail corner.

### 3. INSTRUMENTATION

A major concern in using total head probes at transonic speeds is the possibility of flow interference; thus, every attempt was made to reduce exposure of the probing mechanism to the main flow field although some disruption of the base flow was unavoidable. The

probe support designed for these tests is shown in Figure 4. The probe tip moves through a  $7^\circ$  arc during traverse of 2.5 cm normal to the surface. Four probes were used in these tests. The radii of the probes, from their open tip to the center of rotation on the probe support, are given in Table 1. Note that separate probe supports and their position on the indexing rack were adjusted so that the movement of the tip was always normal to the cylindrical or conical surface, depending on which tap position was being probed. The probe travel was controlled by an electric motor driving a micrometer lead screw

TABLE 1: Probe Radii.

Tap No.	X/L	$R_{probe}$ cm
3	0.870	20.52
4	0.902	20.52
6	0.924	16.79
7	0.946	16.79
8	0.967	14.35
9	0.989	11.93

located within the model. The speed control allowed positioning within  $\pm 0.03$  mm, when measured directly outside the wind tunnel. The position of the probe arm was detected using a Linear Variable Differential Transducer (LVDT). The entire system was statically calibrated using an optical cathetometer which provided an overall position accuracy of  $\pm 0.1$  mm. The probe tip was electrically insulated so that wall contact provides a reference position for calibration in the tunnel.

The probe tip was made of crushed hypodermic tubing with an opening of approximately 0.25 by 2 mm. The minimum distance from the wall for the probe centerline was 0.15 mm. Total head pressures were measured with a 0 to 70 kPa transducer and static pressure measurements required a 0-35 kPa transducer within the model.

#### 4. DATA REDUCTION

The total head pressure probe measurements were divided by the local wall static pressure obtained without a probe on the model and this ratio was used to obtain a local Mach number using either isentropic formulas in subsonic flow or the Rayleigh Pitot formula in supersonic flow. This procedure assumes that the pressure is constant across the boundary layer which is a valid approximation except just downstream of the boattail corner where an expansion wave affects the static pressure distribution. The Mach numbers were then used to calculate the local flow velocity assuming a linear Crocco temperature-velocity relationship. This assumption was checked against a similar calculation using a constant stagnation temperature and a nonlinear form of Crocco's temperature-velocity relationship. No significant differences were observed.

Additional details regarding the data reduction are given in the Appendix. This

appendix also contains tabulations of the reduced data, most of which have not been documented previously.

### III. COMPUTATIONAL TECHNOLOGY

The complete set of three dimensional, time dependent, generalized geometry, thin-layer, Navier-Stokes equations for general spatial coordinates  $\xi$ ,  $\eta$ ,  $\zeta$  can be written as<sup>1</sup>:

$$\partial_\tau \hat{q} + \partial_\xi \hat{E} + \partial_\eta \hat{F} + \partial_\zeta \hat{G} = Re^{-1} \partial_\zeta \hat{S} \quad (1)$$

where

$$\begin{aligned} \xi &= \xi(x, y, z, t) && \text{- longitudinal coordinate} \\ \eta &= \eta(x, y, z, t) && \text{- circumferential coordinate} \\ \zeta &= \zeta(x, y, z, t) && \text{- nearly normal coordinate} \\ \tau &= t && \text{- time} \end{aligned}$$

and

$$\begin{aligned} \hat{q} &= \frac{1}{J} \begin{bmatrix} \rho \\ \rho u \\ \rho v \\ \rho w \\ e \end{bmatrix} & \hat{E} &= \frac{1}{J} \begin{bmatrix} \rho U \\ \rho u U + \xi_x p \\ \rho v U + \xi_y p \\ \rho w U + \xi_z p \\ (e + p)U - \xi_t p \end{bmatrix} \\ \hat{F} &= \frac{1}{J} \begin{bmatrix} \rho V \\ \rho u V + \eta_x p \\ \rho v V + \eta_y p \\ \rho w V + \eta_z p \\ (e + p)V - \eta_t p \end{bmatrix} & \hat{G} &= \frac{1}{J} \begin{bmatrix} \rho W \\ \rho u W + \zeta_x p \\ \rho v W + \zeta_y p \\ \rho w W + \zeta_z p \\ (e + p)W - \zeta_t p \end{bmatrix} \end{aligned} \quad (2)$$

and where

$$\hat{S} = \frac{1}{J} \begin{bmatrix} 0 \\ \mu(\zeta_x^2 + \zeta_y^2 + \zeta_z^2)u_\zeta + \frac{\mu}{3}(\zeta_x u_\zeta + \zeta_y v_\zeta + \zeta_z w_\zeta)\zeta_x \\ \mu(\zeta_x^2 + \zeta_y^2 + \zeta_z^2)v_\zeta + \frac{\mu}{3}(\zeta_x u_\zeta + \zeta_y v_\zeta + \zeta_z w_\zeta)\zeta_y \\ \mu(\zeta_x^2 + \zeta_y^2 + \zeta_z^2)w_\zeta + \frac{\mu}{3}(\zeta_x u_\zeta + \zeta_y v_\zeta + \zeta_z w_\zeta)\zeta_z \\ \{(\zeta_x^2 + \zeta_y^2 + \zeta_z^2)[\frac{\mu}{2}(u^2 + v^2 + w^2)_\zeta \\ + \frac{\kappa a_\zeta^2}{Pr(\gamma - 1)}] \\ + \frac{\mu}{3}(\zeta_x u + \zeta_y v + \zeta_z w)(\zeta_x u_\zeta + \zeta_y v_\zeta + \zeta_z w_\zeta)\} \end{bmatrix} \quad (3)$$

In equation (1), the thin-layer approximation is used and the viscous terms involving velocity gradients in both the longitudinal and circumferential directions are neglected. The viscous terms are retained, however, for velocity gradients in a direction nearly normal to the surface where large flowfield gradients exist. The formulation retains the momentum equation in all three coordinate directions. The retention of all three equations allows for the approximate computation of three-dimensional and separated flow and thus differs significantly from the boundary layer equations.

For this computation, the diffusion coefficients  $\mu$  and  $\kappa$  contain molecular and turbulent parts. The turbulent contributions are supplied through an algebraic eddy-viscosity hypothesis which has been developed by Baldwin and Lomax.<sup>19</sup>

The velocities in the  $\xi$ ,  $\eta$ , and  $\zeta$  coordinate directions can be written

$$\begin{aligned} U &= \xi_t + u\xi_x + v\xi_y + w\xi_z \\ V &= \eta_t + u\eta_x + v\eta_y + w\eta_z \\ W &= \zeta_t + u\zeta_x + v\zeta_y + w\zeta_z \end{aligned}$$

which represent the contravariant velocity components.

The Cartesian velocity components ( $u$ ,  $v$ ,  $w$ ) are retained as the dependent variables and are nondimensionalized with respect to  $a_\infty$  (the free stream speed of sound). The local pressure is determined using the relation

$$p = (\gamma - 1)[e - 0.5\rho(u^2 + v^2 + w^2)] \quad (4)$$

where  $\gamma$  is the ratio of specific heats. Density ( $\rho$ ) is referenced to  $\rho_\infty$  and the total energy ( $e$ ) to  $\rho_\infty a_\infty^2$ . The transport coefficients are also nondimensionalized with respect to the corresponding free stream variables. Thus the Prandtl number which appears in  $\hat{S}$  is defined as  $Pr = c_{p\infty}\mu_\infty/\kappa_\infty$ .

At zero angle of attack, these equations are equivalent to the azimuthally invariant (or generalized axisymmetric) flow, in which the  $\partial_\eta \hat{F}$  term can be simplified as  $\hat{H}^{20}$

$$\partial_r \hat{q} + \partial_\xi \hat{E} + \partial_\zeta \hat{G} + \hat{H} = \frac{1}{Re} \partial_\zeta \hat{S} \quad (5)$$

where

$$\hat{H} = \frac{1}{J} \begin{bmatrix} 0 \\ 0 \\ \rho V [R_\xi (U - \xi_t) + R_\zeta (W - \zeta_t)] \\ -\rho V R (V - \eta_t) - p/R \\ 0 \end{bmatrix} \quad (6)$$

then equation (1) is simplified and contains only two spatial derivatives but does retain all three momentum equations thus allowing a degree of generality over the standard axisymmetric equations. In particular, the circumferential velocity is not assumed to be zero and cross flow components can be computed.

The numerical algorithm used is the Beam-Warming<sup>18</sup> fully implicit, approximately factored, finite difference scheme. The algorithm can be first or second order accurate in time and second or fourth order accurate in space. Since the interest here is only in the steady-state solution, equations (1 and 5) are solved in a time asymptotic fashion and first order accurate time differencing is used. The spatial accuracy is fourth order. Details of the algorithm are described in References 1, 18 and 34.

To suppress high frequency oscillations that appear in regions containing severe pressure gradients e.g., shocks or stagnation points, artificial dissipation terms are added for both zero and four degree angle of attack computations. In the present application, a switching dissipation model<sup>30</sup> is used which is a blend of second and fourth order dissipation terms. Incorporation of this dissipation model has resulted in improvements to the quality of the results and has made the code more robust.

## 1. COMPUTATIONAL GRIDS

In order to perform the computation, the flow field domain about the model shown in Figure 3, must be discretized. The computational grid used was obtained from a hyperbolic grid generation program developed by Nietubicz, et al.<sup>35</sup>

For zero angle of attack and Mach number 0.94, the computations were performed with three different grids depending on how the projectile base is modeled.

1) In this case, the base is modeled consistent with the actual flight projectile without a sting. Figures 5 and 6 show the computational grid in this form. The generated grid consists of two segments. First, the grid in the outer region, which is generated by a hyperbolic solver, runs all the way to the downstream boundary. This outer region covers

all regions up to the body of the projectile and up to a straight cylinder extending behind the base. The minimum spacing at the wall is 0.00002 model diameters, which results in at least two grid points being in the laminar sublayer. Second, the grid behind the base (i.e., within the cylinder downstream of the base region) is simply obtained by extending the outer grid lines as straight lines perpendicular to line AB (Figure 6) down to the centerline. An exponential stretching with minimum spacing of 0.00002 calibers is used on both sides of the line AB, thus maintaining a smooth variation of the grid across the cut. The longitudinal spacing is increased downstream of the base. The number of grid points above and below the line AB is thus the same in the longitudinal direction.

In the outer region, there are 170 grid points in the longitudinal direction with clustering taking place at  $X/D=3.762$  and 5.3, the expected locations of appreciable change in the flow variables. In the base region, 41 points downstream of the base are used. The number of grid points in the normal direction is 70. Therefore, the total number of grid points is  $211 \times 70$  in these computations.

2) A second grid shown in Figures 7 and 8 has been used which incorporates a sting at the base of the same diameter as that used to support the model in the experiments. The grid in the longitudinal direction is wrapped around the projectile base and on to the supporting sting. The grid points in front of, and above, the base are identical to those in the first grid. The fifty points between the base (5.8 caliber) and the sting (5.816 caliber), in the longitudinal direction, approximate the sharp corner at the base. The size of the numerical grid is  $212 \times 70$ .

3) In the third case, illustrated in Figures 9 and 10, the 0.5 caliber, 7.00 degree, boattail is extended by a 7.64 degree conical surface for a distance of 2.52 calibers until the diameter of the extended base is decreased to the diameter of the straight sting (0.2 calibers in diameter). The surface line of this model is then parallel to the approximate wake direction. This approximation is made according to the free-flight shadowgraphs for projectile shapes at transonic speeds. All the grid points in front of, and above, the base are identical to the points of the previous two computational grids.

The numerical experiments designed to investigate the sensitivity of the results to the grid were performed using the third base model. Grids using  $170 \times 70$  and  $170 \times 50$  longitudinal and normal points, respectively, are employed for the verification of the grid independence in the normal direction. Grids using  $170 \times 50$ ,  $187 \times 50$ ,  $205 \times 50$ , and  $245 \times 50$  longitudinal and normal points, respectively, are used for the verification in the longitudinal direction. More longitudinal points (17 and 35) are inserted near the nose corner ( $0.45 < X/L < 0.57$ ) to the  $170 \times 50$  grid, thus forming grids of  $187 \times 50$  and  $205 \times 50$ . In addition 40 more points are placed near the boattail corner and on the boattail ( $0.89 < X/L < 1.0$ ) to the  $205 \times 50$  grid, so that a  $245 \times 50$  grid is formed.

These two-dimensional computations were performed on the BRL Cray-XMP computer. These computations required 1.4 million words of memory storage and 1.09 CPU seconds per time step for the  $187 \times 50$  grid (i.e., approximately  $10^{-4}$  cpu seconds/grid point /time step). About 2000 time steps were needed to reach converged, steady-state solutions. Convergence was assumed when the largest residual of the set of dependent variables was reduced three orders of magnitude.

When computing the angle of attack case, the extended boattail grid was employed in many of the runs in order to take advantage of its more rapid rate of convergence. As will be seen, this grid provides results which are in satisfactory agreement with the results using grids with better modeling of the base, except for the last 2 per cent of the model length. There were 39 points in the circumferential direction although only points on a half plane were computed because of symmetry (5 degree increments plus two reflected points). A single run of the 170x50x75 grid was performed to check the independence of grid spacing in the circumferential direction. The three-dimensional computations were performed on the BRL Cray-2 computer. Ten million words of memory storage and 120 CPU seconds per time step were required for the 170x50x39 grid (i.e.,  $4 \times 10^{-4}$  cpu seconds/grid point/time step). About 2500 time steps were needed to approach steady-state solutions.

#### IV. EFFECT OF DIFFERENT GRIDS

Surface pressure coefficients, velocity profiles and Mach number contours are compared to illustrate the effects of the three different base region grids.

##### 1. SURFACE PRESSURE COEFFICIENTS

Figure 11 compares the surface pressure coefficients along the projectile for the extended boattail grid together with the experimental data of Danberg<sup>2</sup> and Miller.<sup>4</sup> The computed surface pressure coefficients obtained with these simpler grids of 170 longitudinal points with 50 or 70 points radially agree almost perfectly everywhere except for very slight differences at  $X/L=0.63$  where a substantial change of the flowfield occurs. This indicates that the solution is essentially independent of the numerical grid in the normal direction. The velocity profiles generated with these grids were found to be identical near the wall and showed small differences of 1.5 per cent in the far field.

Figure 12 illustrates the effect on the pressure coefficient distribution of employing the three different base grid configurations in the computations. The excellent agreement of the computed surface pressure coefficients obtained by the grid with the real base (211x70 grid) and by the grid where the points wrapped around the base and sting (212x70 grid) shows that both grids yield essentially the same result ahead of the base. The extended boattail computation gives a slightly lower pressure coefficient in the region  $0.96 < X/L < 1.0$ . As might be expected, the grid with the sting is in good agreement with the measurements. It is apparent that the small diameter sting has little effect on the boattail pressure because of the good agreement with the flat base computation.

It is noted that there are significant discrepancies, in the previous two figures, between computations and measurements near the nose corner ( $0.5 < X/L < 0.6$ ). The discontinuity in slope and curvature at the corner causes an appreciable pressure coefficient change at that location. Therefore, 17 and 35 more longitudinal points were added between  $0.45 < X/L < 0.57$  to the 170x50 grid and in both cases much improved agreement was obtained with the data of Miller as shown in Figure 13.

In order to check whether the grid spacing is fine enough near the boattail corner and on the boattail, 40 points have been inserted between the longitudinal points of the 205x50 grid to form a 245x50 grid. No visible differences were found between the surface pressure coefficients obtained from these two grids near the boattail corner and on the boattail (see Figure 13). Oscillations are observed in the pressure distribution when the finest grid is used. It is believed that too large a time step was used in that case. It is concluded that the 187x50 grid is sufficient to get substantially improved surface pressure coefficients for the region  $0.5 < X/L < 1.0$ ; and that 170x50 grid points are sufficient for region  $0.8 < X/L < 1.0$  in two dimensional computations. Moreover, the comparisons also imply that the inaccuracy produced by the coarse grid near the nose corner does not propagate downstream and interfere with the results near and on the boattail.

## 2. VELOCITY PROFILE

The experimental velocity profile for the most rearward station,  $X/L=0.989$ , is shown in Figure 14 along with computed profiles for the three basic grid configurations. For the extended boattail grid, relatively large differences of the order of 3 to 5 per cent are observed relative to the experimental data. However, when the base region is more accurately modeled, good agreement is obtained. The velocity profile obtained by employing the extended boattail is seen to have the largest disagreement with data, as expected, because of its poor modeling of the near wake flow field.

## 3. MACH NUMBER CONTOURS

Comparing the Mach number contours (Figure 15, 16, and 17) for these three computational grids, overall agreement is obtained for locations ahead of the base although completely different patterns are shown behind the base. A very slight shift in the shock location caused by the presence of the supporting sting in the computations can be observed if Figures 15 and 16 are superimposed. Comparing Figures 16 and 17, it is found that the Mach number contours in front of the base for the extended boattail are identical except for the outermost Mach number contour.

It may be concluded from the overall comparisons of the results for different computational grids that the differences are generally small. However, to correctly predict the boattail pressure distribution for the final two or three per cent of the body, the base region needs to be correctly modeled.

## V. COMPARISON OF NUMERICAL PREDICTION WITH EXPERIMENT

### 1. PRESSURE COEFFICIENT DISTRIBUTION AT $\alpha = 0^\circ$

For Mach number 0.94, the surface pressure coefficients in the longitudinal direction agree well with Danberg's and Miller's experimental data except for the locations very close to the shock and the base corner ( $X/L=0.967$  and  $0.989$ ) (see Figure 12). For Mach number 0.97, excellent agreement between measured and computed values are obtained except for the location next to the base ( $X/L=0.989$ ), if the extended boattail grid is employed (Figure 18). Comparison of the results at Mach numbers 0.94 and 0.97 show that the pressure coefficient drops less, recovers at a slower rate, but reaches to a higher value after the ogive-cylinder junction ( $X/L$  around 0.58) for Mach number 0.97.

### 2. VELOCITY PROFILES AT $\alpha = 0^\circ$

The velocity profiles at Mach number 0.94 and zero angle of attack are shown in Figure 19 for the wrapped around grid configuration. This grid is the most realistic for the sting supported wind tunnel model. Note that there is generally good agreement between the experiment and the prediction for most stations.

The predicted profile at station  $X/L=0.967$  is approximately 3 per cent higher than the measurements near the outer boundary layer edge. By referring to Figure 12 it can be seen that the predicted static pressure is slightly lower than the data by about 0.04 in pressure coefficient. Because of the steep pressure gradient at this location, a slight difference in the shock wave location, of the order of 0.018 calibers (3.6 mm) could account for the observed pressure and velocity profile results.

Figure 20 compares the measured velocity profiles with the computed values by the extended boattail grid at five axial locations for Mach number 0.97. It shows excellent agreement in front of and behind the boattail corner at  $X/L=0.87, 0.946, 0.967$  but with some discrepancies at  $X/L=0.924, \text{ and } 0.989$ .

The deviations observed at  $X/L=0.924$ , for both the  $M_\infty=0.94$  and  $0.97$  cases, are related to errors in the reduced experimental data. The data were obtained by inserting a probe into the flowfield at that location. Only total head pressures were measured and these data were reduced to velocities assuming constant static pressure, corresponding to the measured wall pressure, across the boundary layer. The presence of the expansion fan from the corner produces a significant variation in the static pressure near the outer edge of the boundary layer which results in the reduced velocity data being too high. The data at the next station, which is well away from the expansion, is in excellent agreement.

The deviations observed at  $X/L=0.989$ , for  $M_\infty=0.97$ , are caused by the upstream effect of modeling the base using the extended boattail. Figure 21 shows that the computed velocity profiles are improved at  $X/L=0.989$  using the wrapped around grid which provides a better evaluation of the conditions at the base. It is also noted that the improved base

model produces only a slight improvement in the agreement at  $X/L=0.967$  which was well predicted by the extended boattail grid. The boattail shock wave has moved downstream of this station at Mach number 0.97. This can be seen clearly by comparing the Mach number contour plots for the wrapped around grid case in Figures 22 and 16. At the higher Mach number the shock wave is about half a caliber aft of the base.

### 3. EFFECT OF ANGLE OF ATTACK

The extended boattail grid (170x50x39) has been used for the Mach number 0.94, four degrees angle of attack results shown in Figure 23. The computations are shown compared to the boattail data of Danberg.<sup>2</sup> The computed pressure coefficients at different orientations start to spread after the expansion wave at the beginning of the boattail and converge toward the same pressure at the base. Note that the pressure increases fastest on the leeside ( $\phi=0.0^\circ$ ). This is consistent with the negative lift generated by the boattail which tends to destabilize the projectile. The spreading of the experimental data is not as large as that computed. The different degree of spreading between measurement and computation suggests that details of the shock-boundary layer interaction region are not being computed correctly.

Figure 24 shows the computed pressure coefficients versus Miller's data employing the 170x50x39 grid. Miller's experimental data are available over the entire body and are generally consistent with Danberg's data in the vicinity of the afterbody. A 245x50x39 grid was employed to increase the accuracy of the solution. A smaller increment between grid points relative to the 170x50x39 grid improves the computational results for the region  $0.5 < X/L < 0.7$ ; but again induces oscillations at several locations caused by too large a time step. No improvement is seen on the boattail. The computational results from grids of various fineness leads to the conclusion that the 170x50x39 grid gives the same quality of results on the boattail, but not at the ogive-cylinder junction, as those from the finer spaced grids.

In comparing Figures 23 and 24 it can be seen that the lee-side pressure rise on the boattail in Miller's data is delayed relative to that of Danberg indicating a somewhat more downstream shock position although the spread in the data with circumferential angle is about the same in both sets of data. By comparing the  $X/L$  position for a lee-side  $C_p$  of -0.3, the shock wave location is estimated to be 0.035 calibers (7 mm) further aft in Miller's experiment. This may be because of the smaller model blockage in the larger NASA Ames wind tunnel.

In comparing the pressure coefficients for zero and four degrees angle of attack (Figure 12 and 24), the major discrepancies between the computation and the experiment occur around two locations, i.e.,  $0.5 < X/L < 0.6$  and  $0.9 < X/L < 1.0$ . On the boattail, the pressure coefficients at four degrees show that the pressure increases faster on the lee-side whereas the windward pressures are about the same as the values at zero angle of attack. Near the ogive-cylinder junction,  $0.5 < X/L < 0.6$ , discrepancies between the computed and measured pressure coefficients are observed which can not be reduced by using grids of finer spacing. However, the variations at different orientations are not large, either in the measurements or in the computations.

Figure 25 plots the velocity profiles at five longitudinal locations for Mach number 0.94 and four degree angle of attack. The agreement between experiment and computation is not as good as it was at zero angle of attack especially for the lee-side. As indicated previously, the agreement is poor where the computed surface pressures are different from the measurements. In addition, the experimental profiles near the wall are steeper than those computed, particularly for the lee-side at stations  $X/L=0.946$ ,  $0.967$ , and  $0.989$ . Even the profiles at  $X/L=0.870$  which is 0.25 calibers in front of the boattail corner are not as well predicted as the zero angle of attack profiles at the same station. It is noted that: (1) a little better prediction of the velocity profiles on the wind-side is obtained than on the lee-side where the boundary layer thickness is larger; (2) the velocity gradients at the wall are all larger for the measured profiles than computed ones. This may imply that the mixing length scale near the wall is not correct in the computation. The model of turbulence which has been employed is based on two-dimensional boundary-layer concepts and, thus, is a potential reason for the discrepancy in this fully three-dimensional flow. However, the magnitude of the velocity and the trends of velocity gradient in the circumferential direction are reasonable.

Figure 26 shows the pressure coefficient along the projectile for Mach number 0.97 at four degrees angle of attack. Note that the number of points near the  $X/L=0.6$  station are insufficient to accurately predict the expansion pressures but that this has no observable effect on the boattail flow. The computed circumferential spread of the data is about the same as in the measurements but the pressure level is different. The position of the boattail shock wave is more forward for the experiment than in the calculation. The velocity profiles at various locations are shown in Figure 27. These profiles are acceptably computed except immediately behind the boattail corner ( $X/L=0.924$ ) and at the most downstream station ( $X/L=0.989$ ). The computed boattail profiles might be improved with a better prediction of the surface pressure distribution and shock wave location.

## VI. CLOSING REMARKS

Transonic computations have been performed on a model, similar to the M549 projectile, using a modified version of the implicit, unsteady, Navier- Stokes code developed by Pulliam and Steger. Studies have been made of the effects of grid configuration and resolution. Comparisons of the results were made with wind tunnel data including pressure distributions and boundary layer profiles at Mach numbers of 0.94 and 0.97 and at  $0.0^\circ$  and  $4.0^\circ$  angle of attack.

The three grid configurations studied include: 1) wrapped around grid with sting corresponding to the wind tunnel situation; 2) segmented grid with flat base as in the flight case; and 3) extended boattail. By comparing the pressure distributions and boundary layer profile characteristics at zero angle of attack, it is found that the wrapped around grid leads to the best agreement with the experimental data. The extended boattail provides adequate accuracy except for the last 2-3 per cent of the body length where the effects of the base corner is of critical importance.

A grid of 187 longitudinal points by 50 radial points is found to provide sufficient

resolution for the pressure distribution over the entire body for the  $\alpha = 0.0^\circ$  cases. Computation of the boattail region is found to be insensitive to the grid resolution at the ogive-cylinder junction region, so that a total of 170 longitudinal points are sufficient to obtain good results in the afterbody region. At an angle of attack of  $4.0^\circ$ , a half plane circumferential grid spacing of 39 points provides satisfactory resolution.

The predicted pressure distribution and velocity profiles at zero angle of attack and at Mach numbers of 0.94 and 0.97 are in good agreement (2-3 per cent) with the wind tunnel experimental data. As already noted, the base configuration must be correctly modeled to accurately compute the region just ahead of the base. Disagreement is observed just aft of the cylinder-boattail corner where the reduced experimental velocity profile data is incorrect because of the influence of the strong expansion waves.

At angle of attack of  $4.0^\circ$ , the computed results are in only fair agreement with the measurements. The trends in the pressure distributions are predicted but the magnitude of the angle of attack effects are over-predicted. This lack of agreement in the pressure is also reflected in the velocity profiles. Although the trends are correct, the experimental profiles are found to have substantially higher velocities near the surface than obtained computationally. The eddy viscosity predicted by the Baldwin-Lomax algebraic turbulence model in regions of strong three dimensional pressure gradients and shock-wave boundary layer interaction is under investigation as a possible explanation.

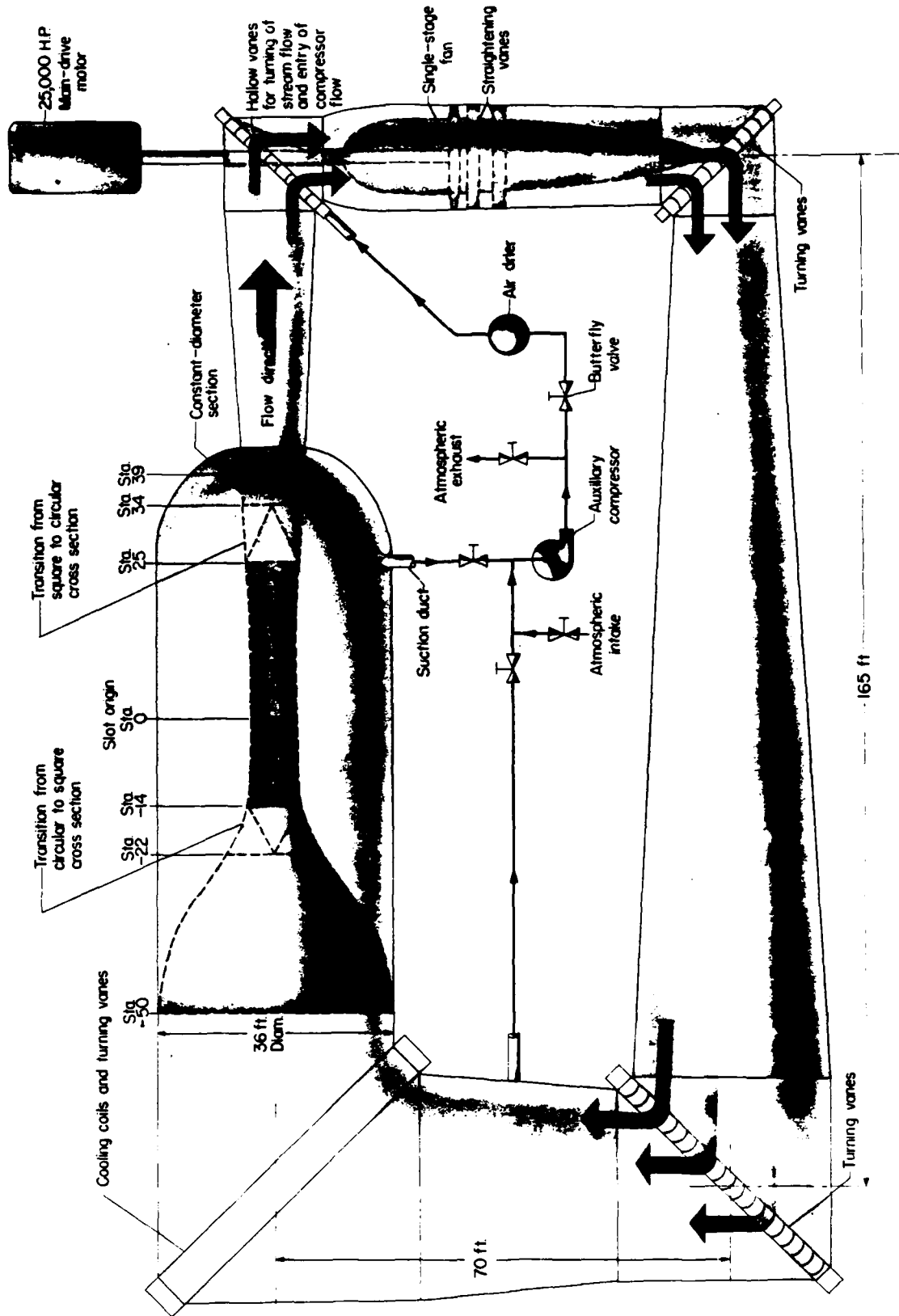


Figure 1. General arrangement of the NASA Langley Research Center transonic pressure tunnel.

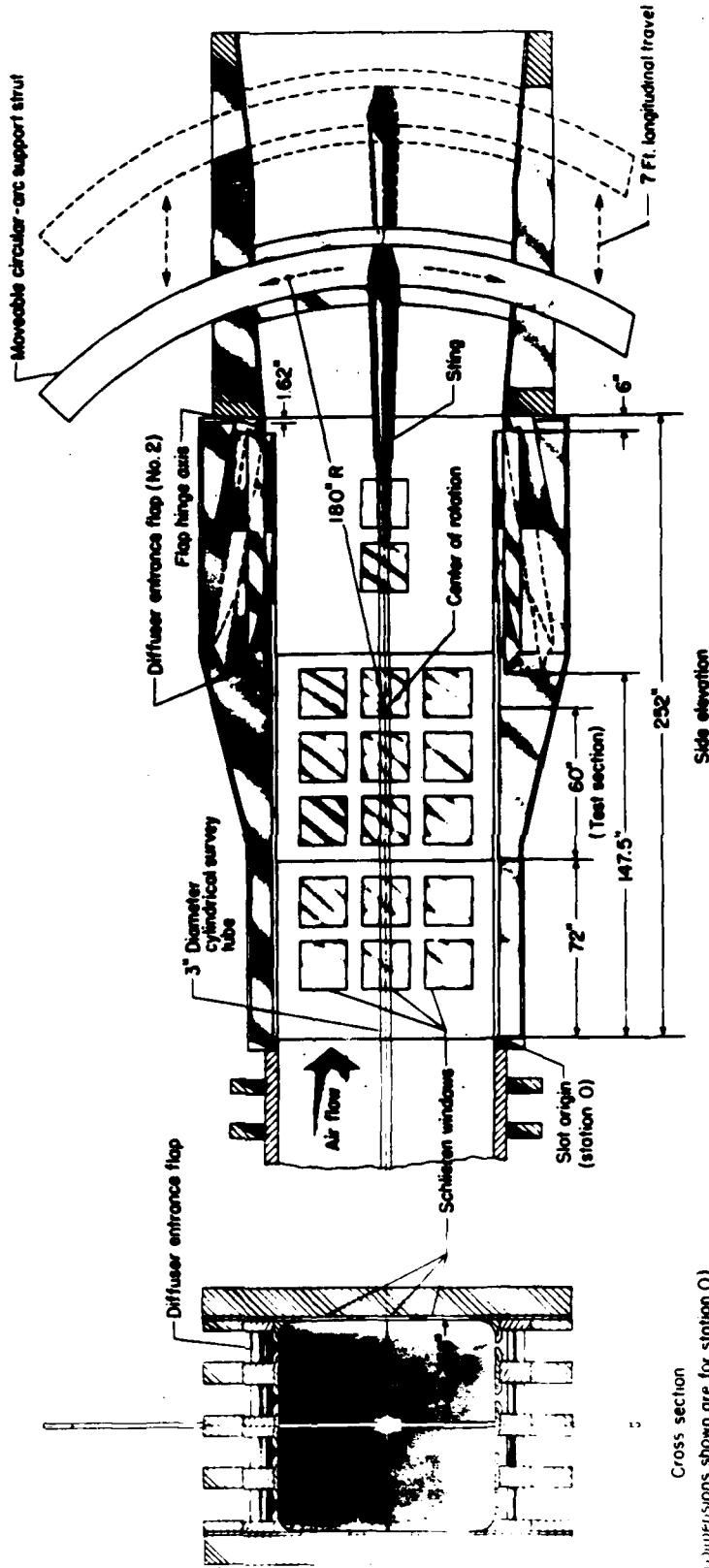


Figure 2. Test section of the NASA Langley Research Center 8 foot transonic pressure tunnel.

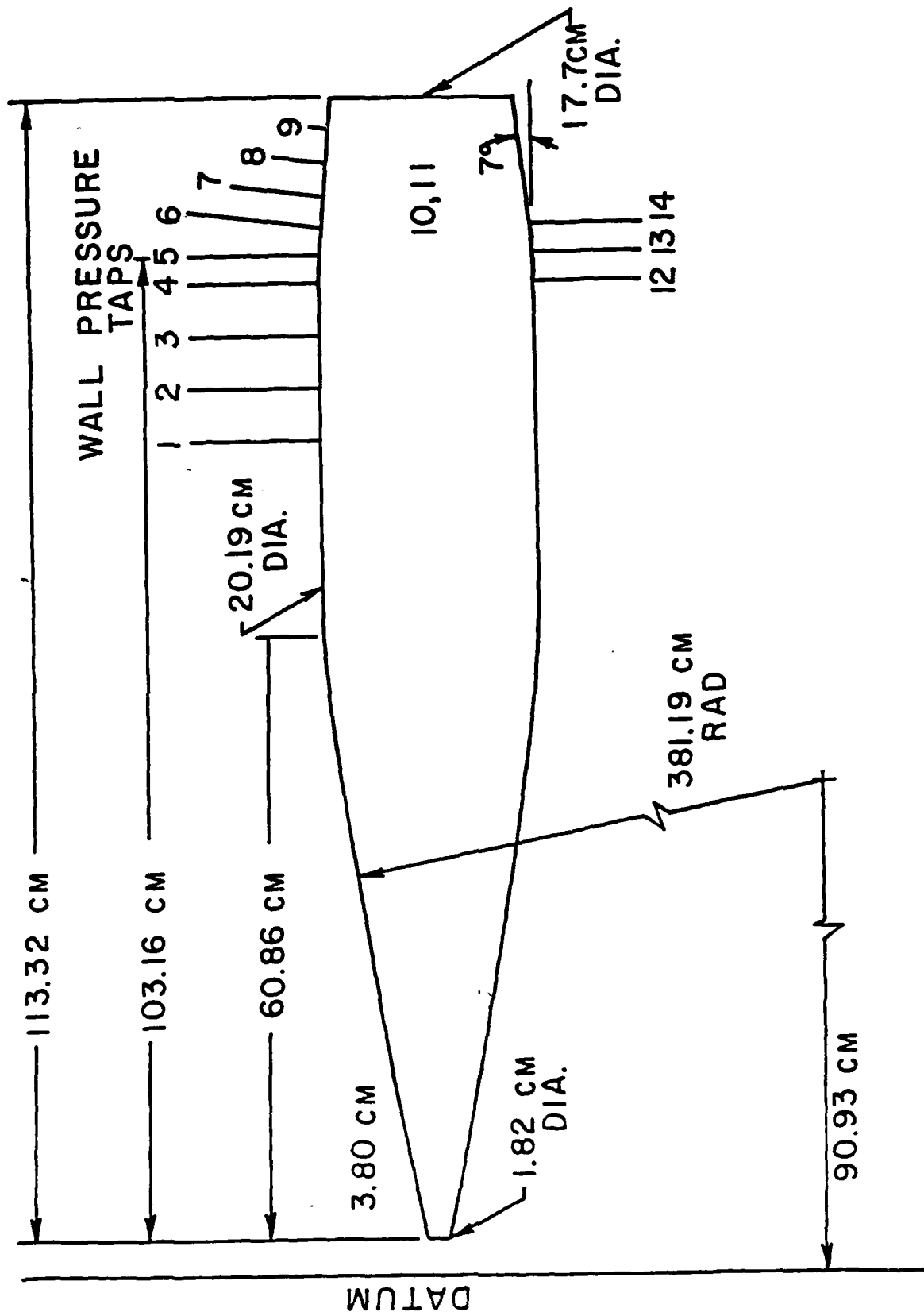


Figure 3. Boattailed model configuration showing dimensions.

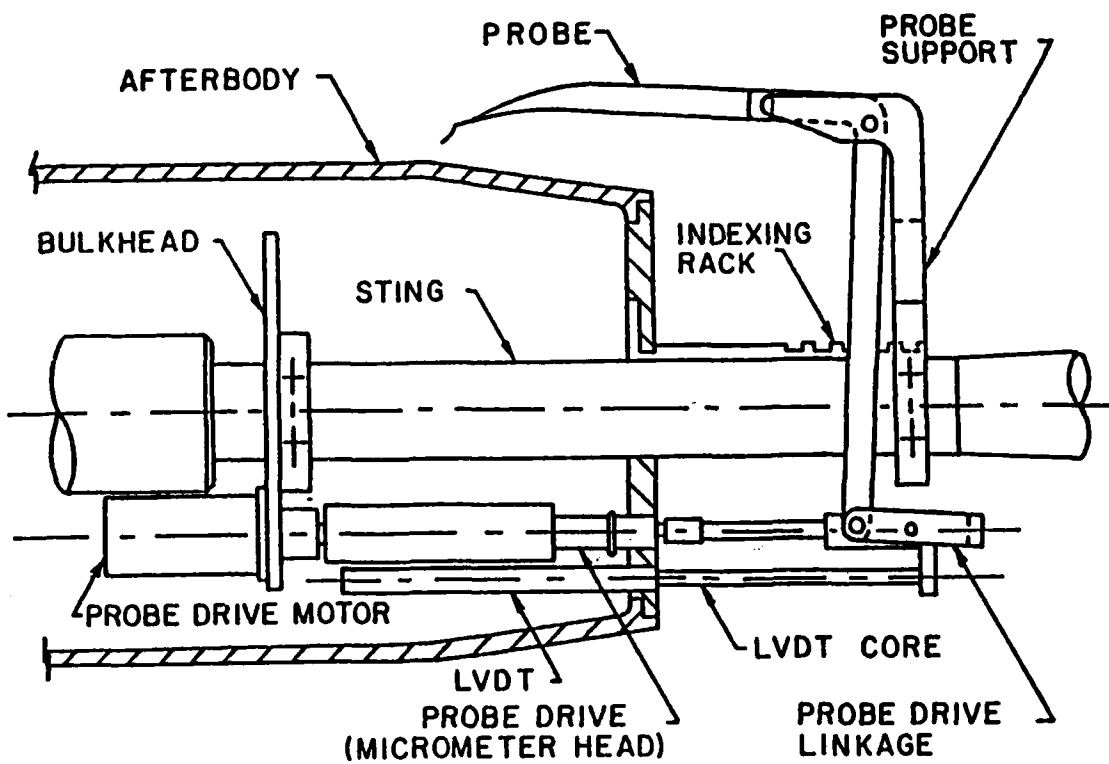


Figure 4. Boundary layer survey mechanism.

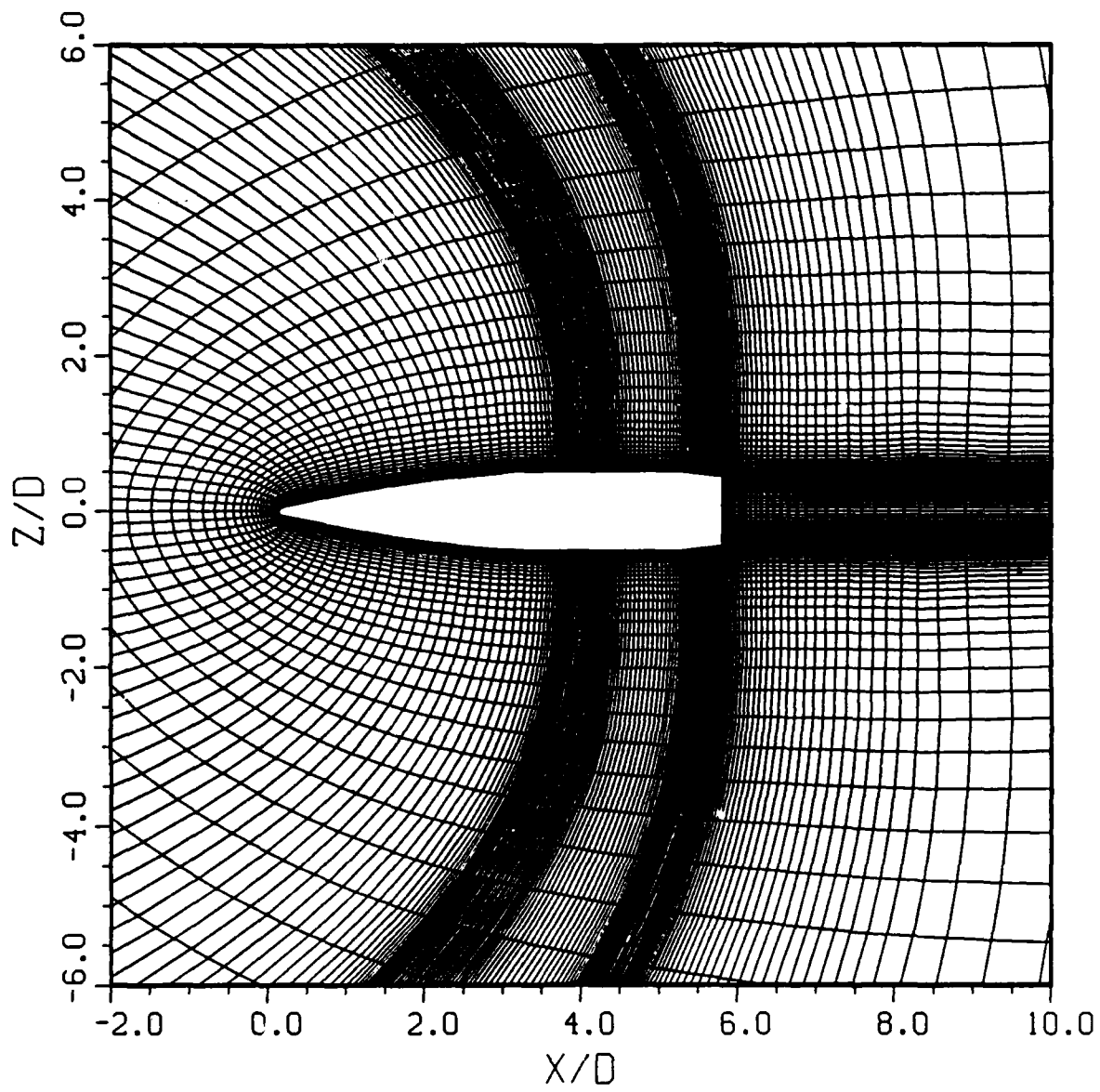


Figure 5. Flat base segmented grid.

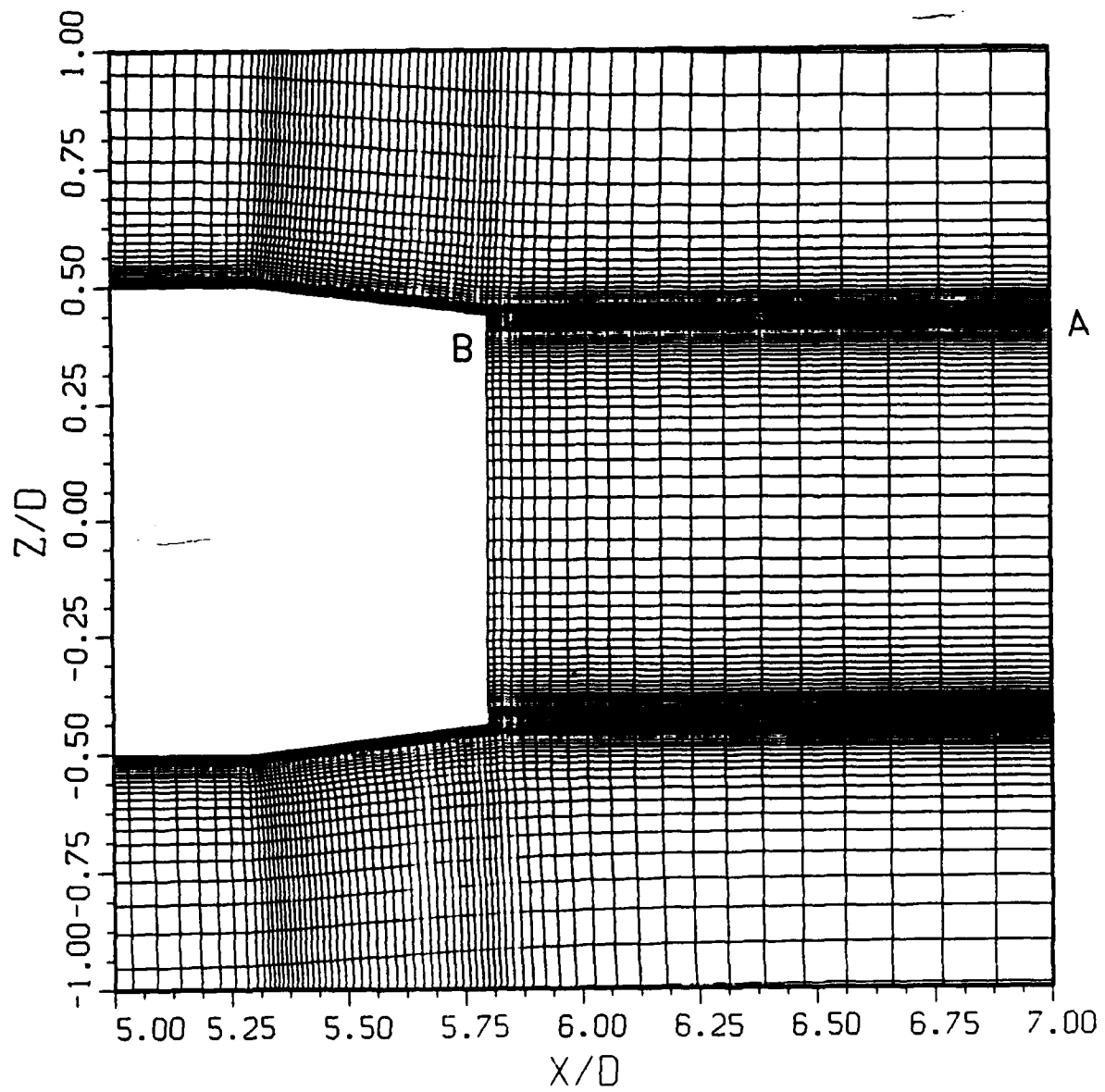


Figure 6. Detail of flat base segmented grid near the base.

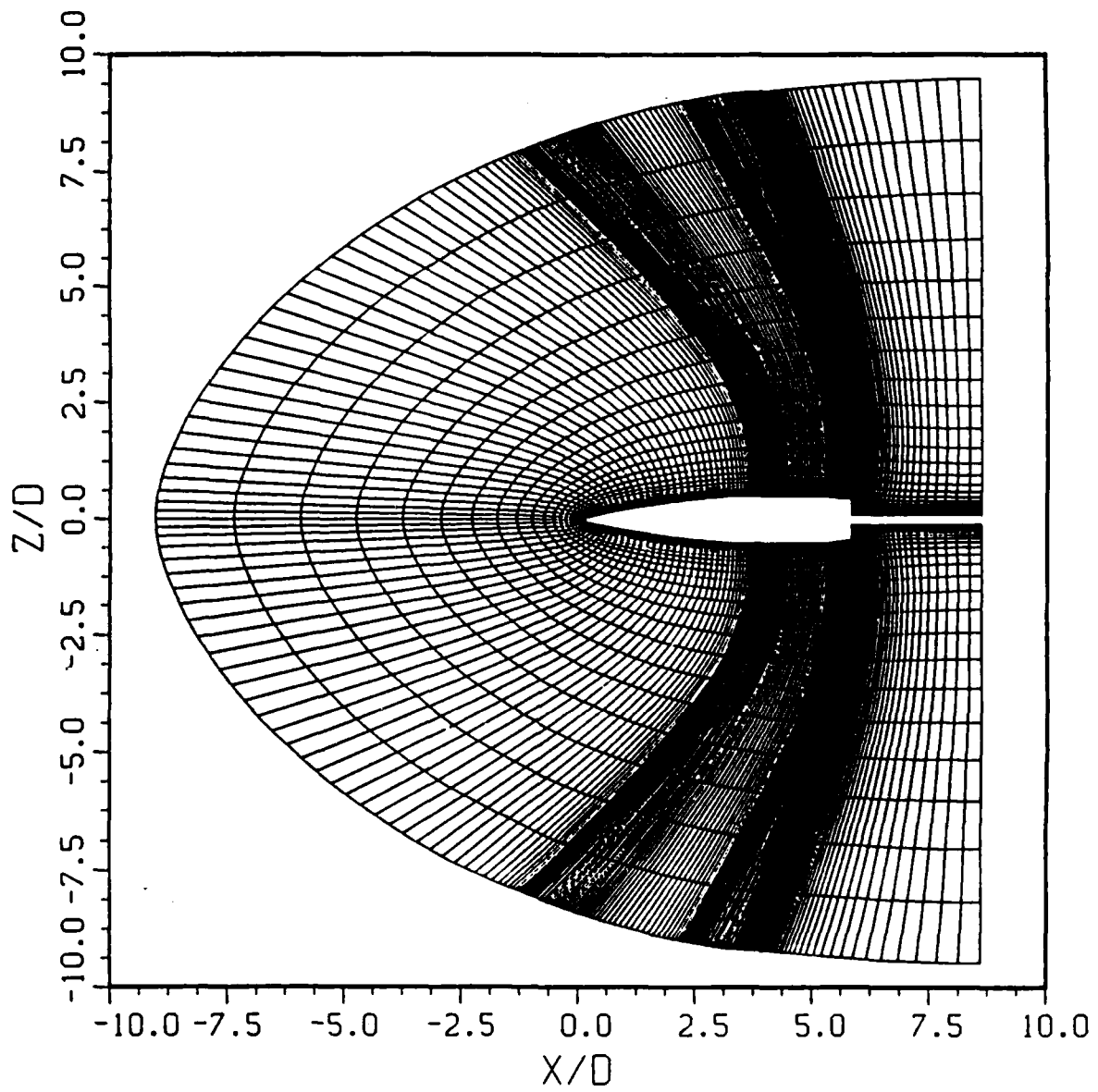


Figure 7. Wrapped around grid with flat base and sting.

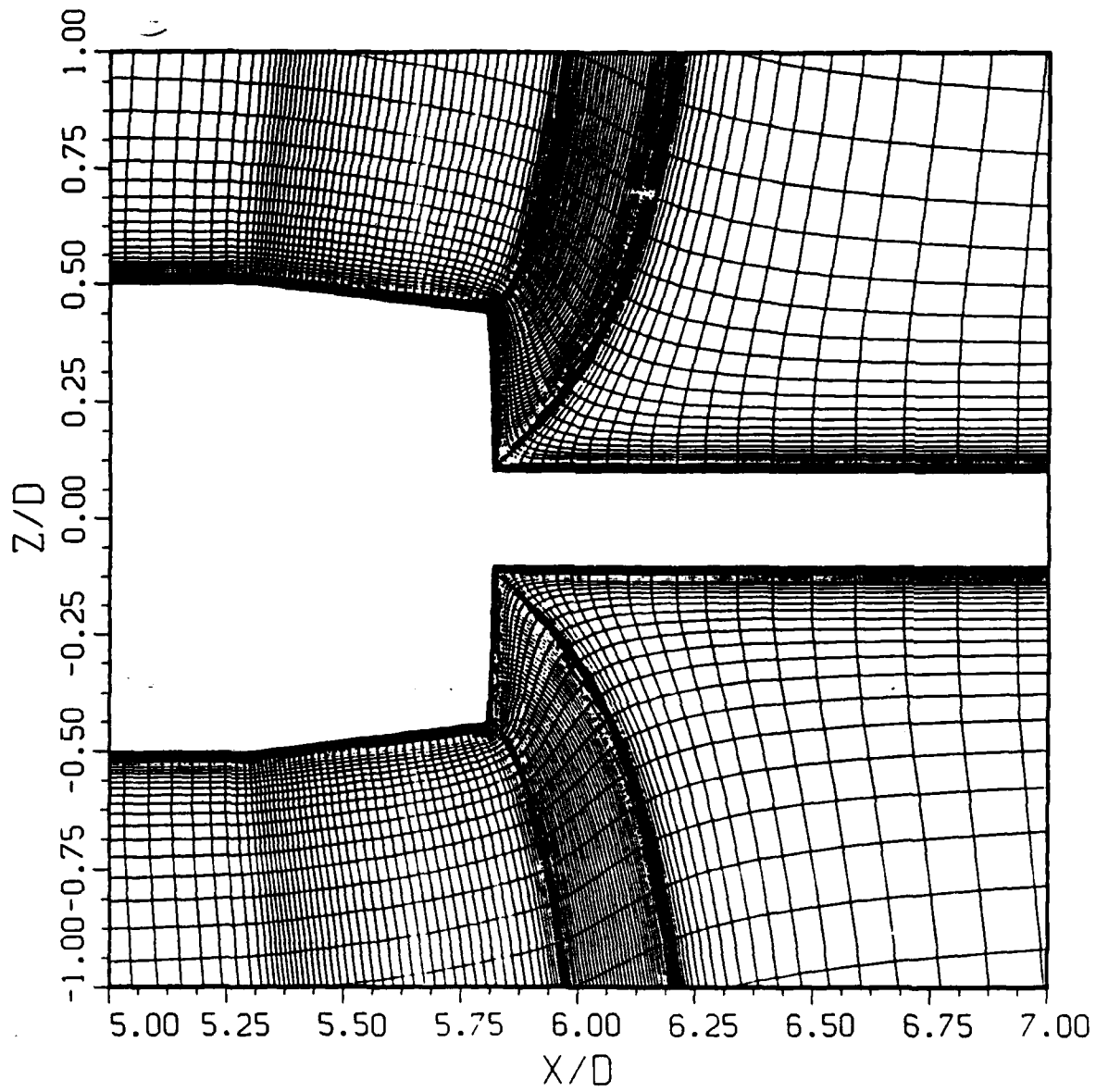


Figure 8. Detail of wrapped around grid near the base.

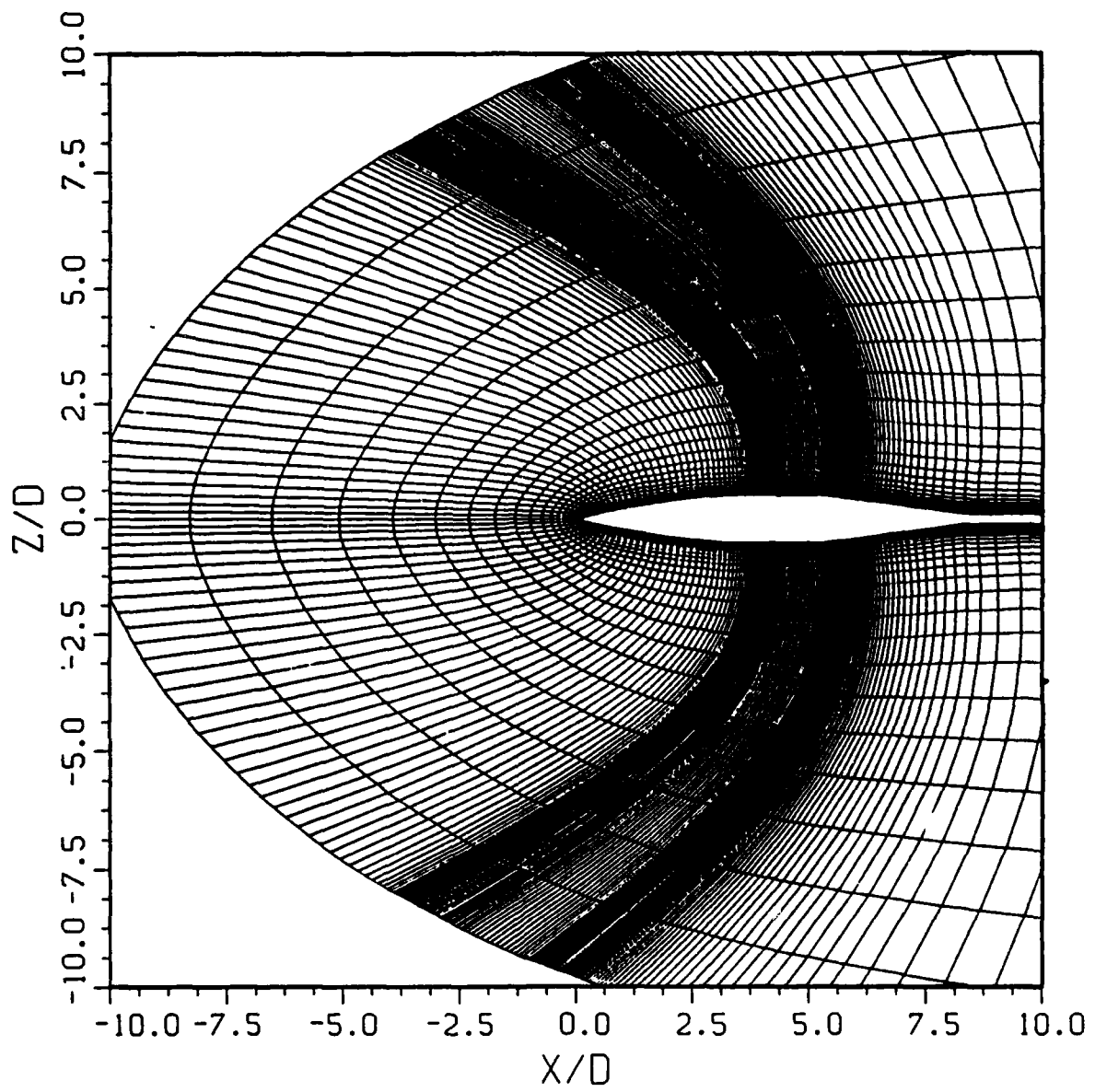


Figure 9. Extended boattail grid.

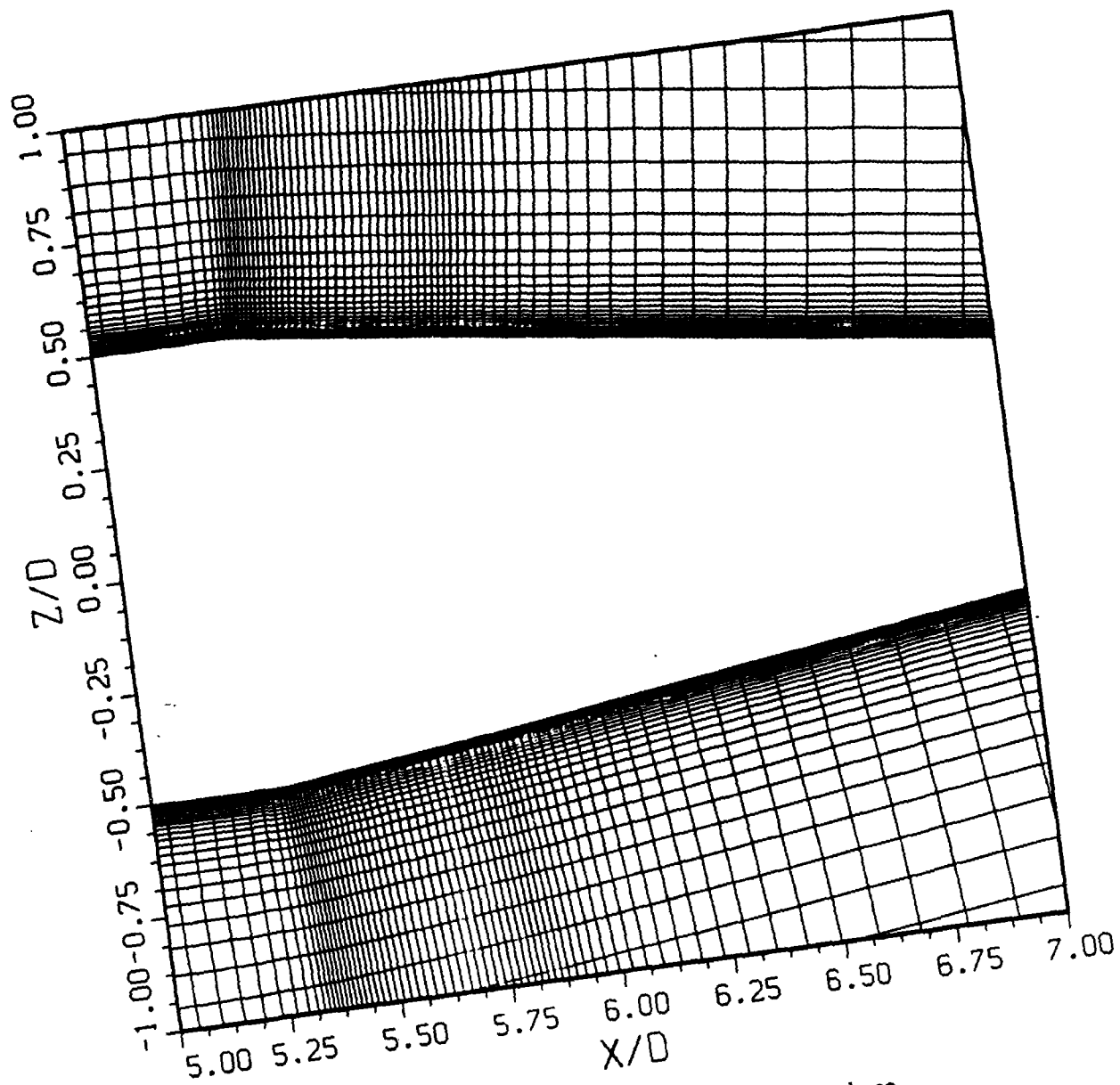


Figure 10. Detail of extended boattail near the base.

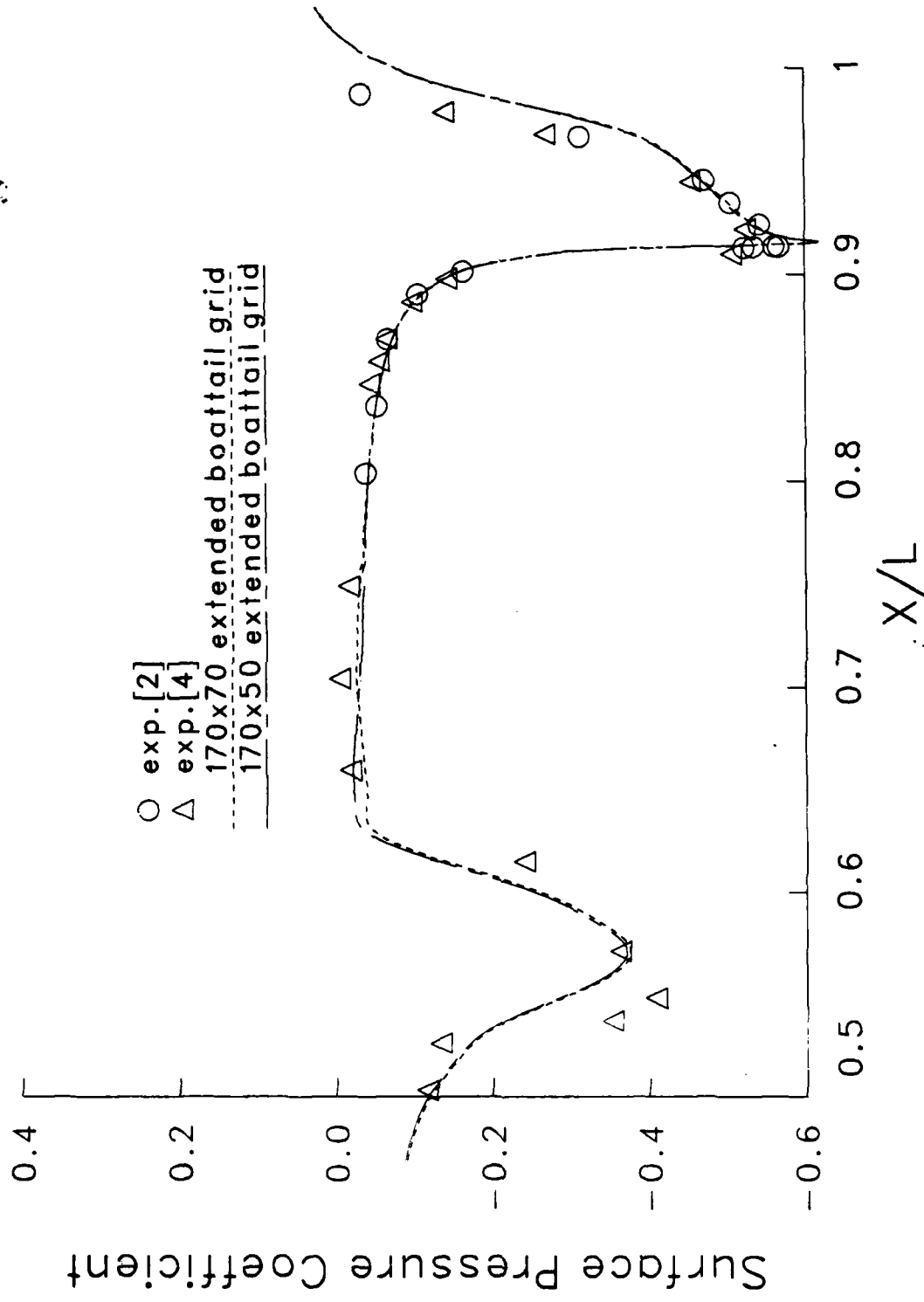


Figure 11. Effect on  $C_p$  of changing the number of normal grid points,  $M_\infty = 0.94$ ,  $\alpha = 0.0^\circ$ .

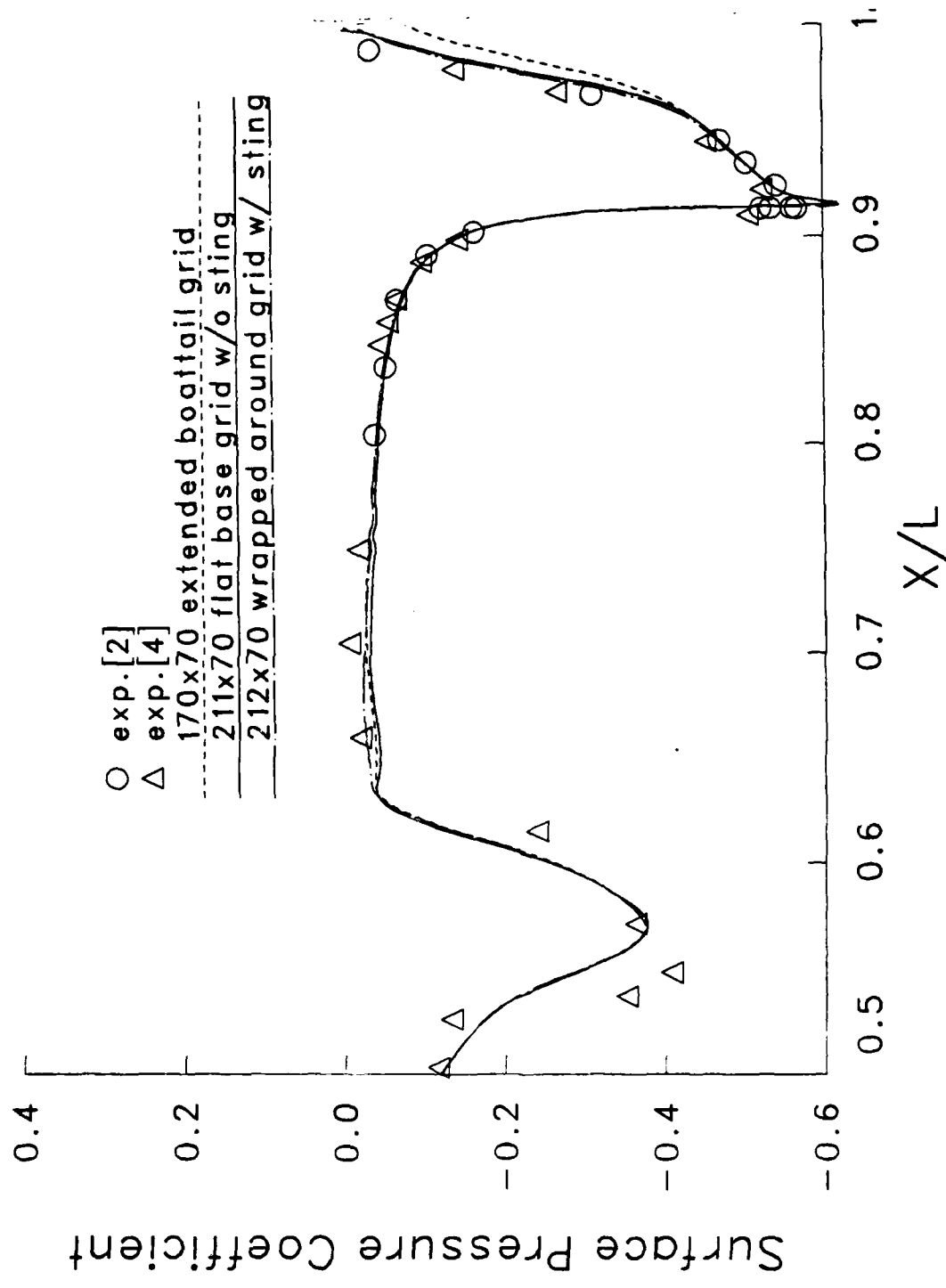


Figure 12. Comparison of surface pressure coefficient distribution for three base grid configurations,  $M_\infty = 0.94$ ,  $\alpha = 0.0^\circ$ .

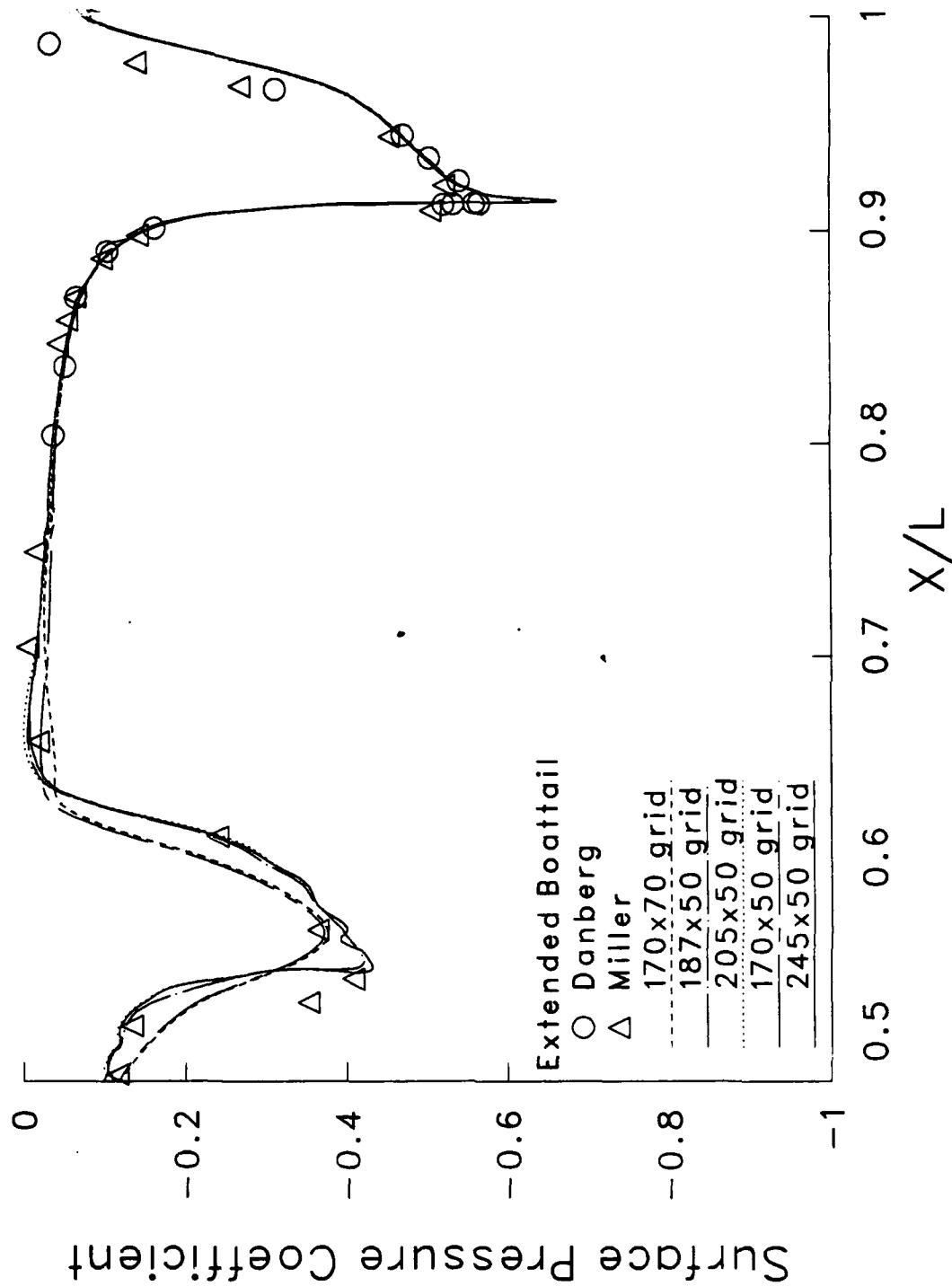


Figure 13. Effect of grid refinement on surface pressure coefficient distribution for extended boattail grid,  $M_{\infty} = 0.94$ ,  $\alpha = 0.0^\circ$ .

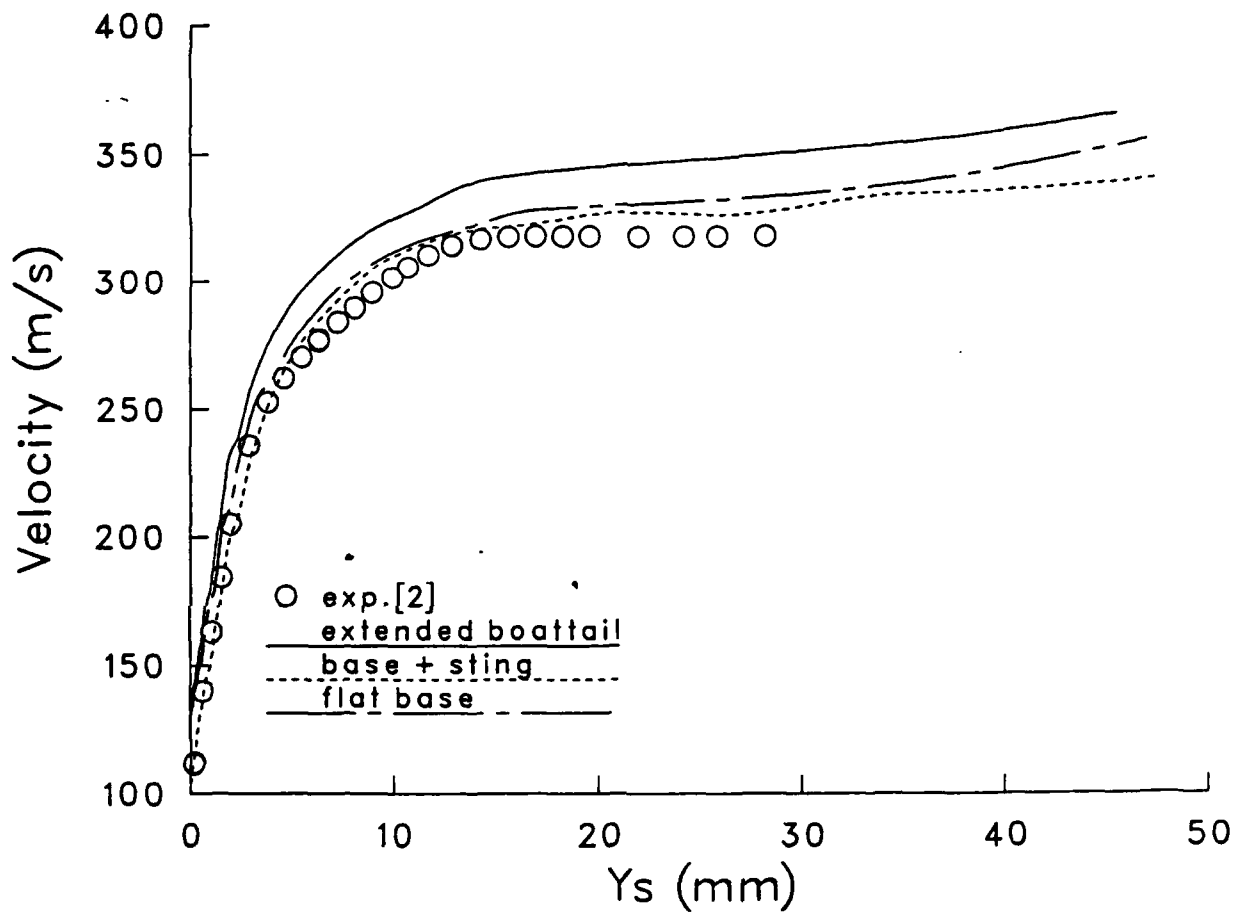


Figure 14. Effect of the three base grids on the velocity profile  
 at  $X/L = 0.989$ ,  $M_\infty = 0.94$ ,  $\alpha = 0.0^\circ$ .

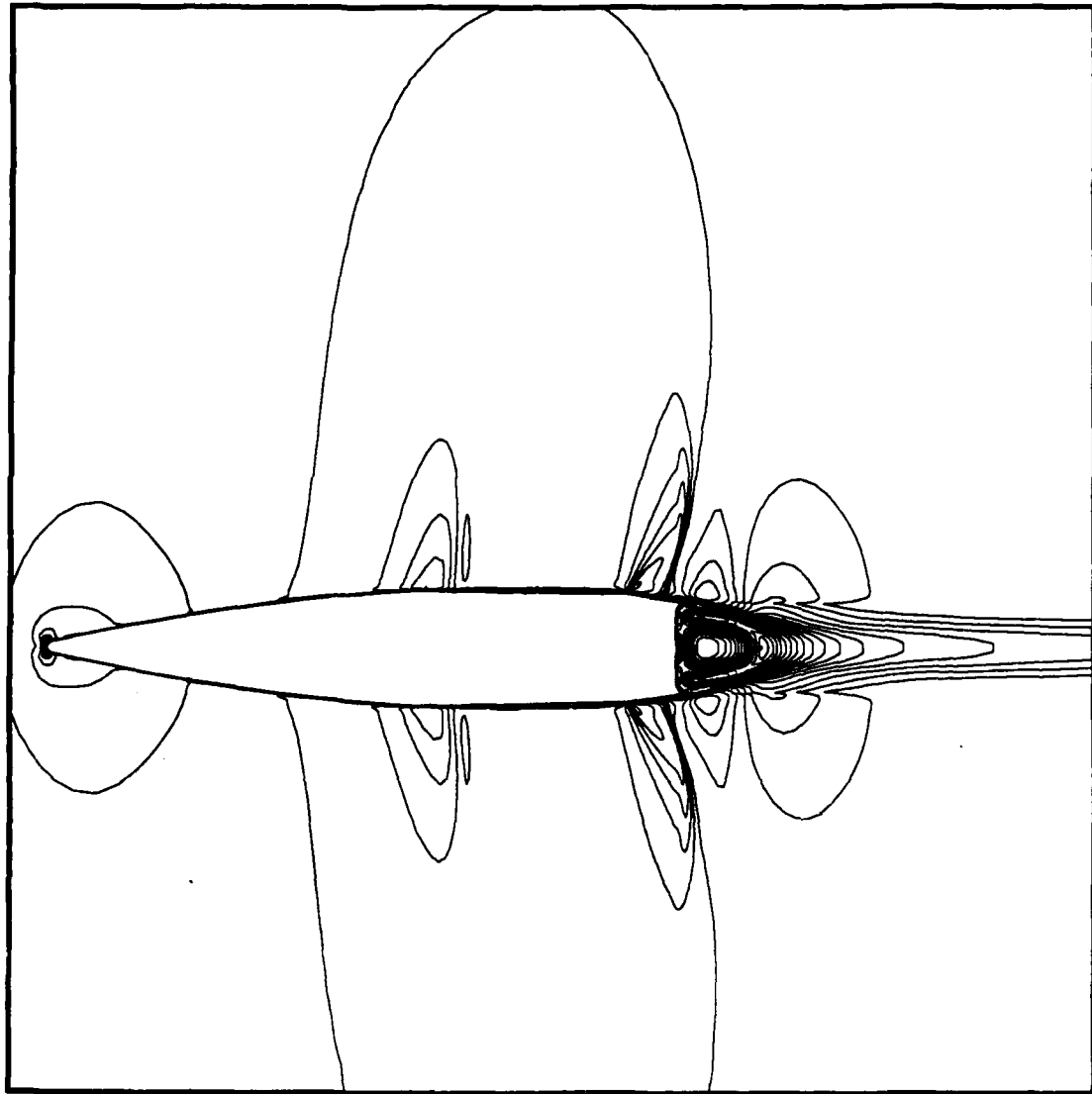


Figure 15. Mach number contours for the flat base grid without a sting.

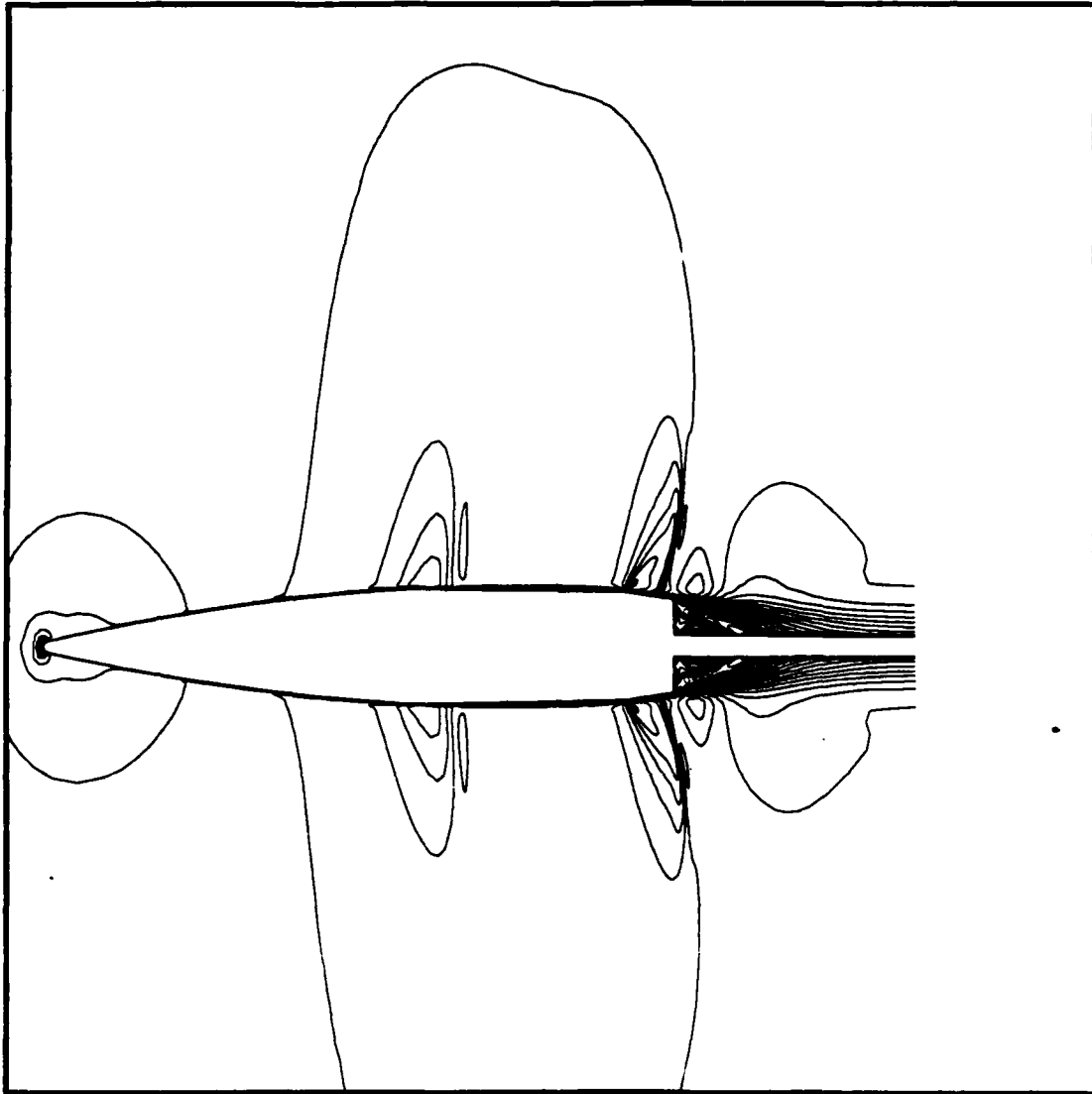


Figure 16. Mach number contours for the wrapped around grid with a sting.

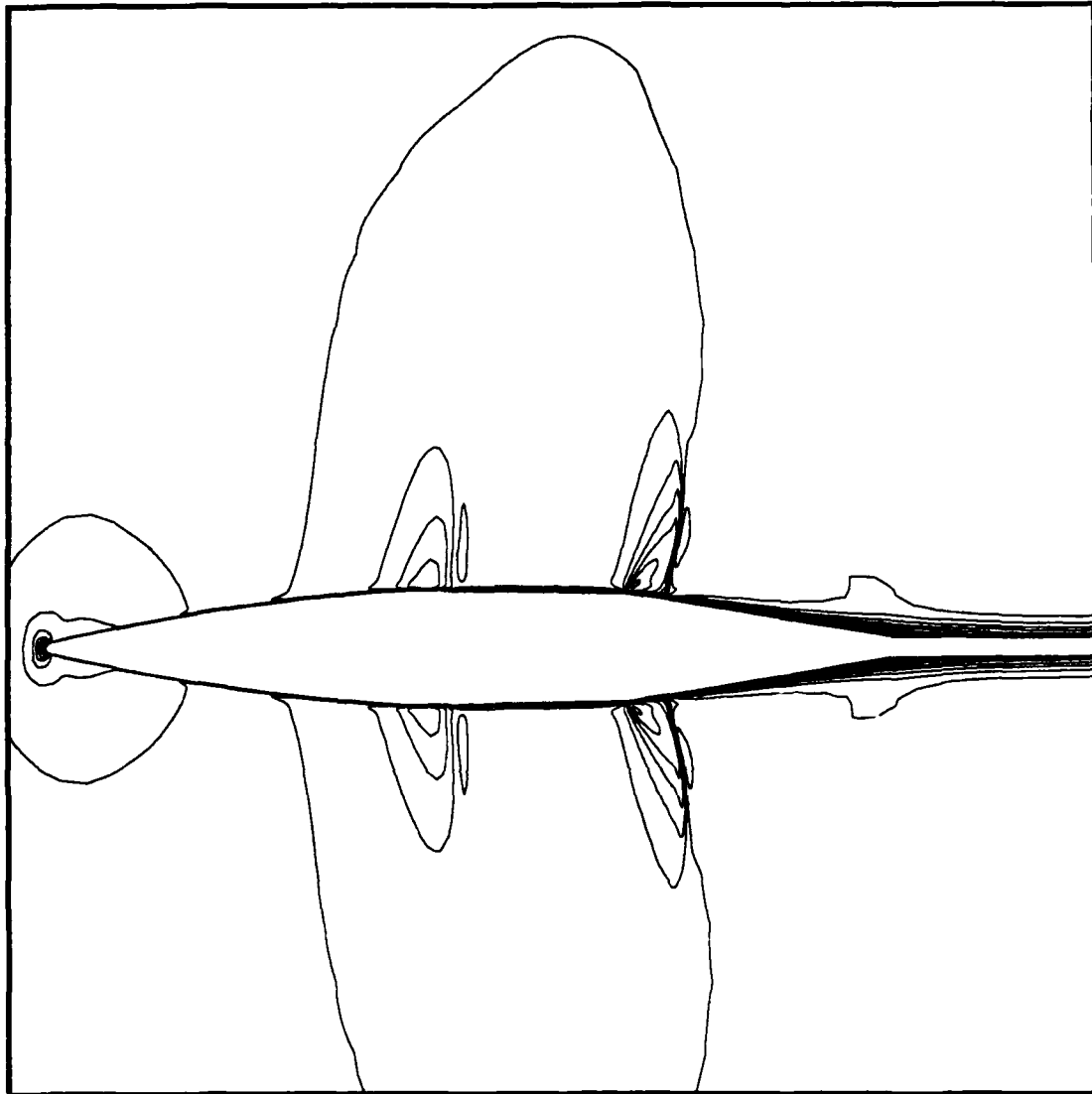


Figure 17. Mach number contours for the extended boattail grid.

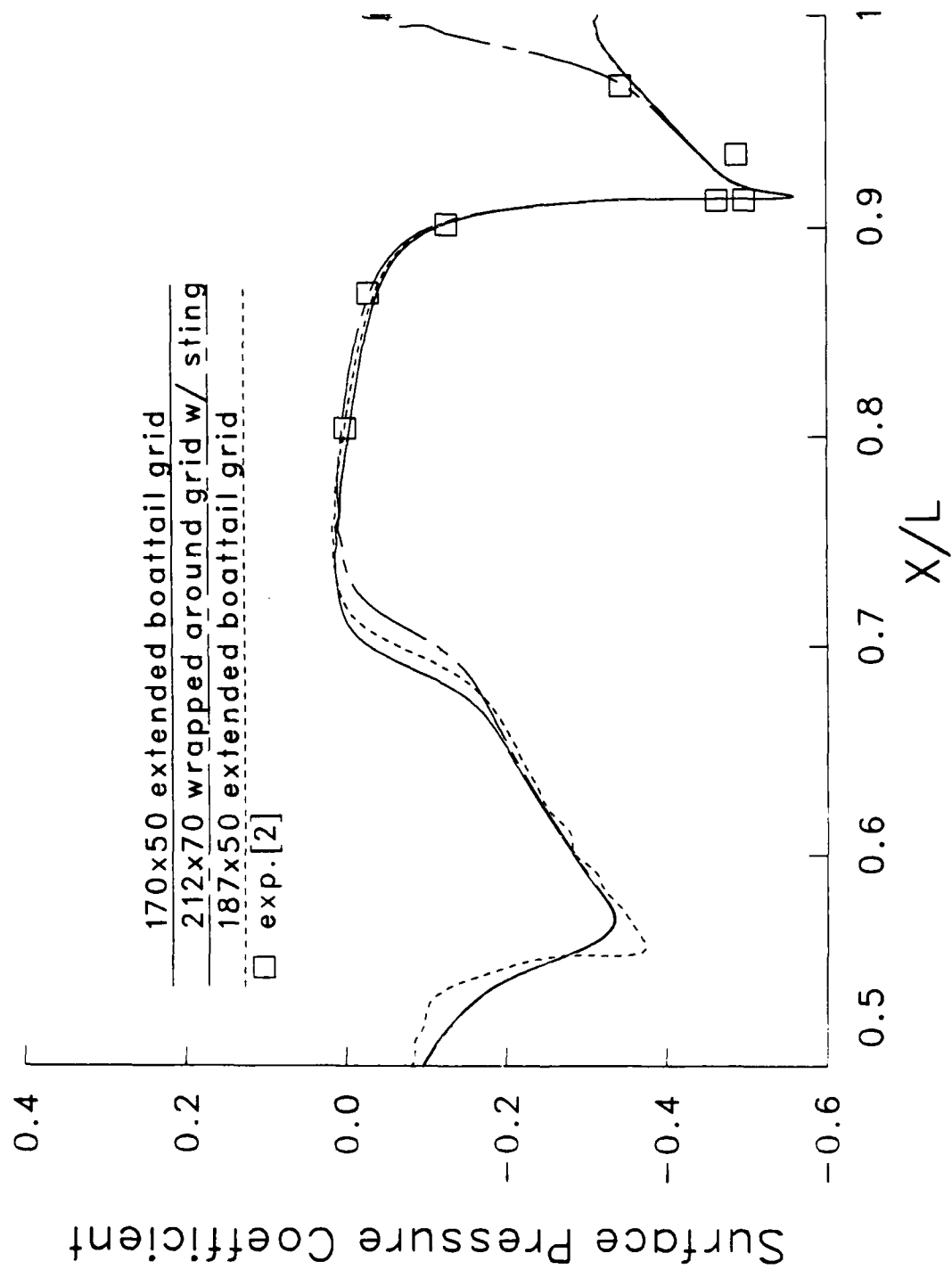


Figure 18. Predict pressure coefficient distributions and comparison with measurements,  $M_\infty = 0.97$ ,  $\alpha = 0.0^\circ$ .

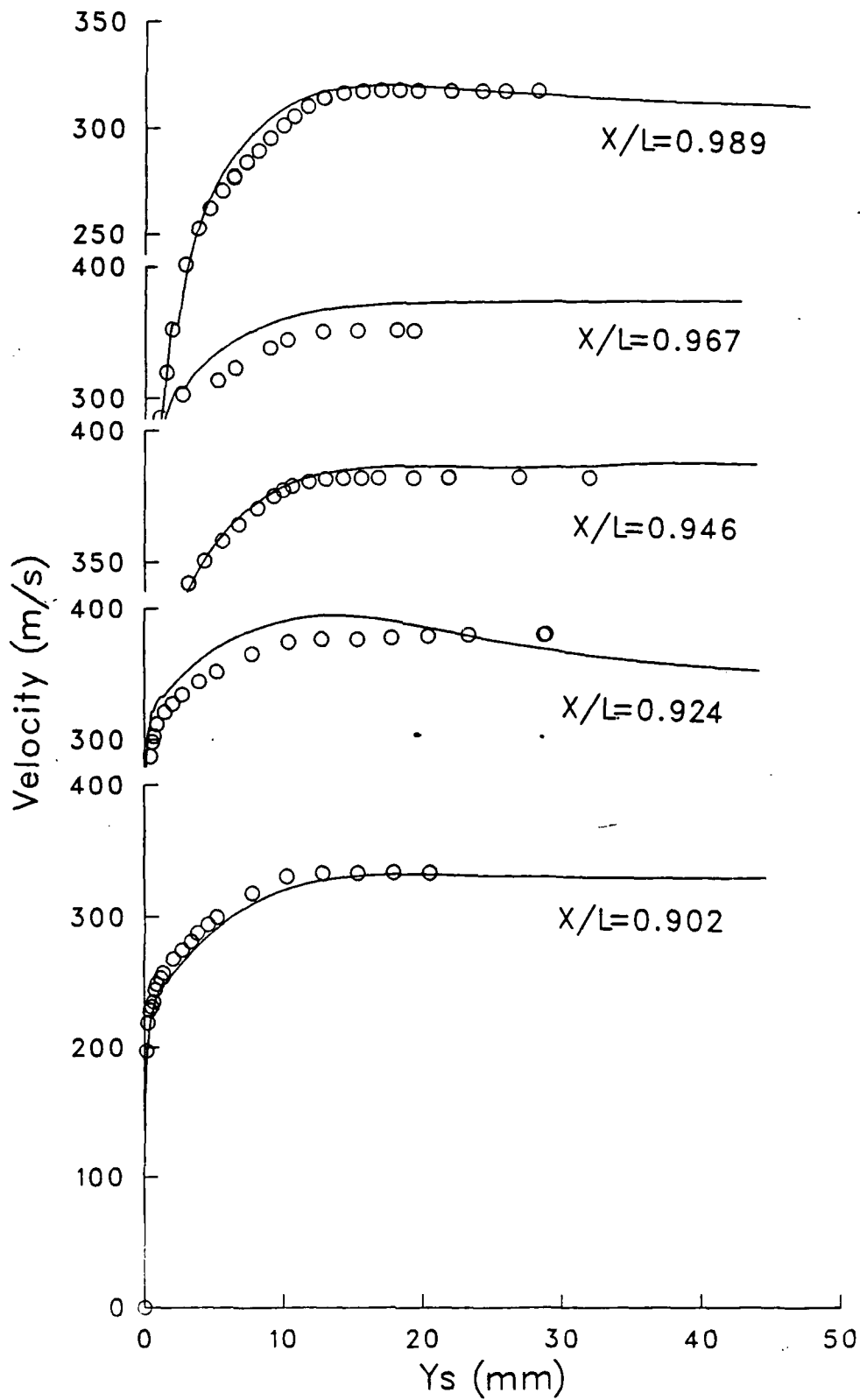


Figure 19. Velocity profiles obtained with the wrapped around grid,  $M_\infty = 0.94$ ,  $\alpha = 0.0^\circ$ .

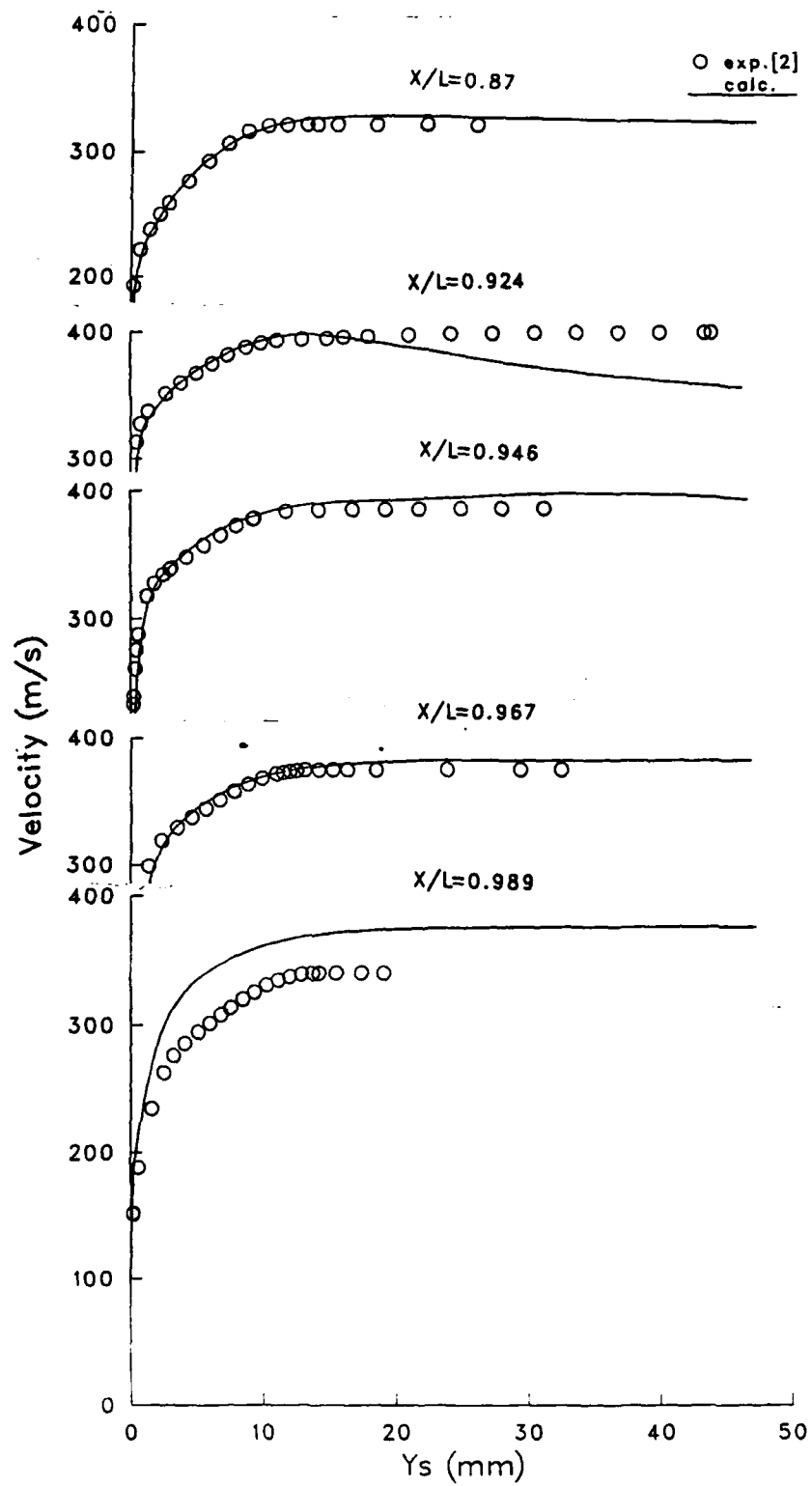


Figure 20. Comparison between predicted and measured velocity profiles using extended boattail grid,  $M_\infty = 0.97$ ,  $\alpha = 0.0^\circ$ .

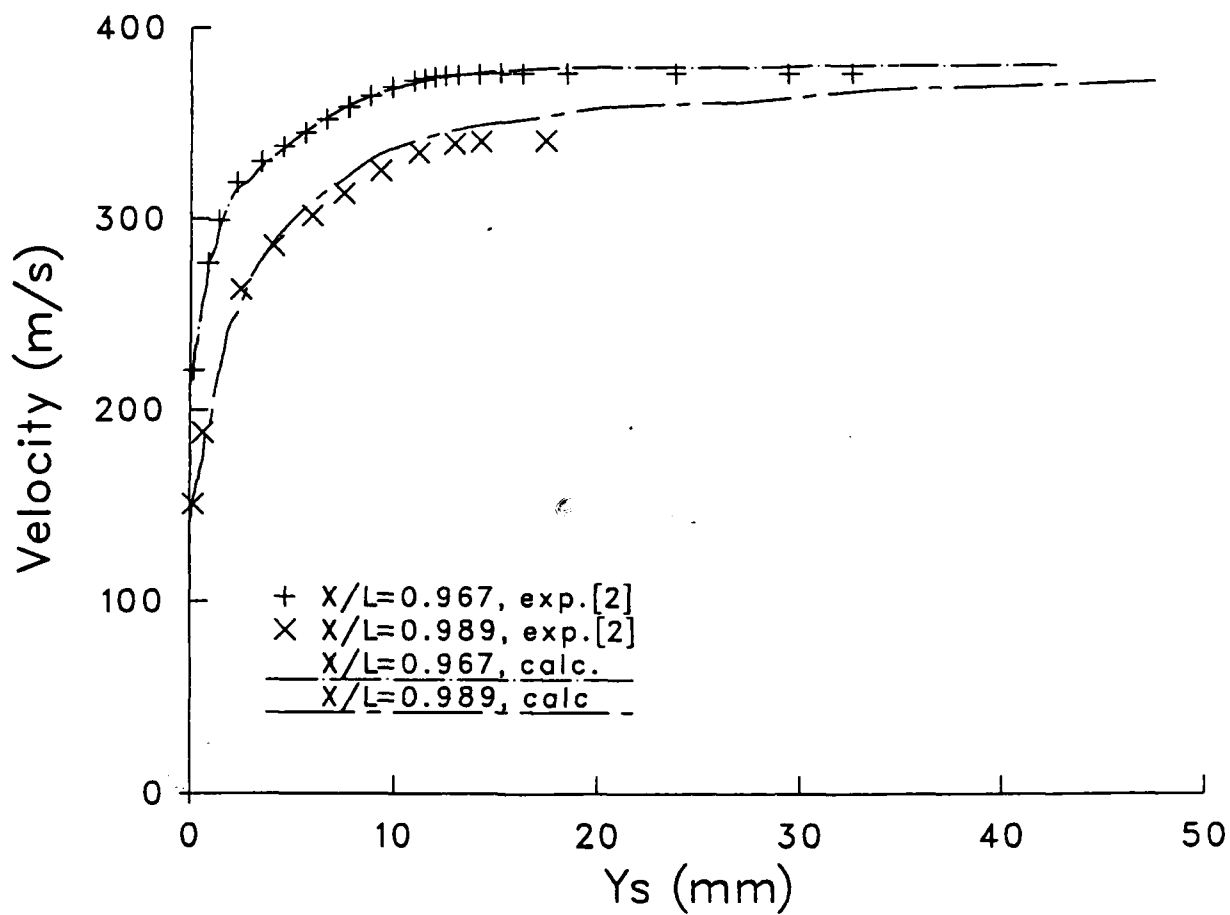


Figure 21. Improved velocity profiles using wrapped around grid at  $X/L = 0.967$  and  $0.989$ ,  $M_\infty = 0.97$ ,  $\alpha = 0.0^\circ$ .

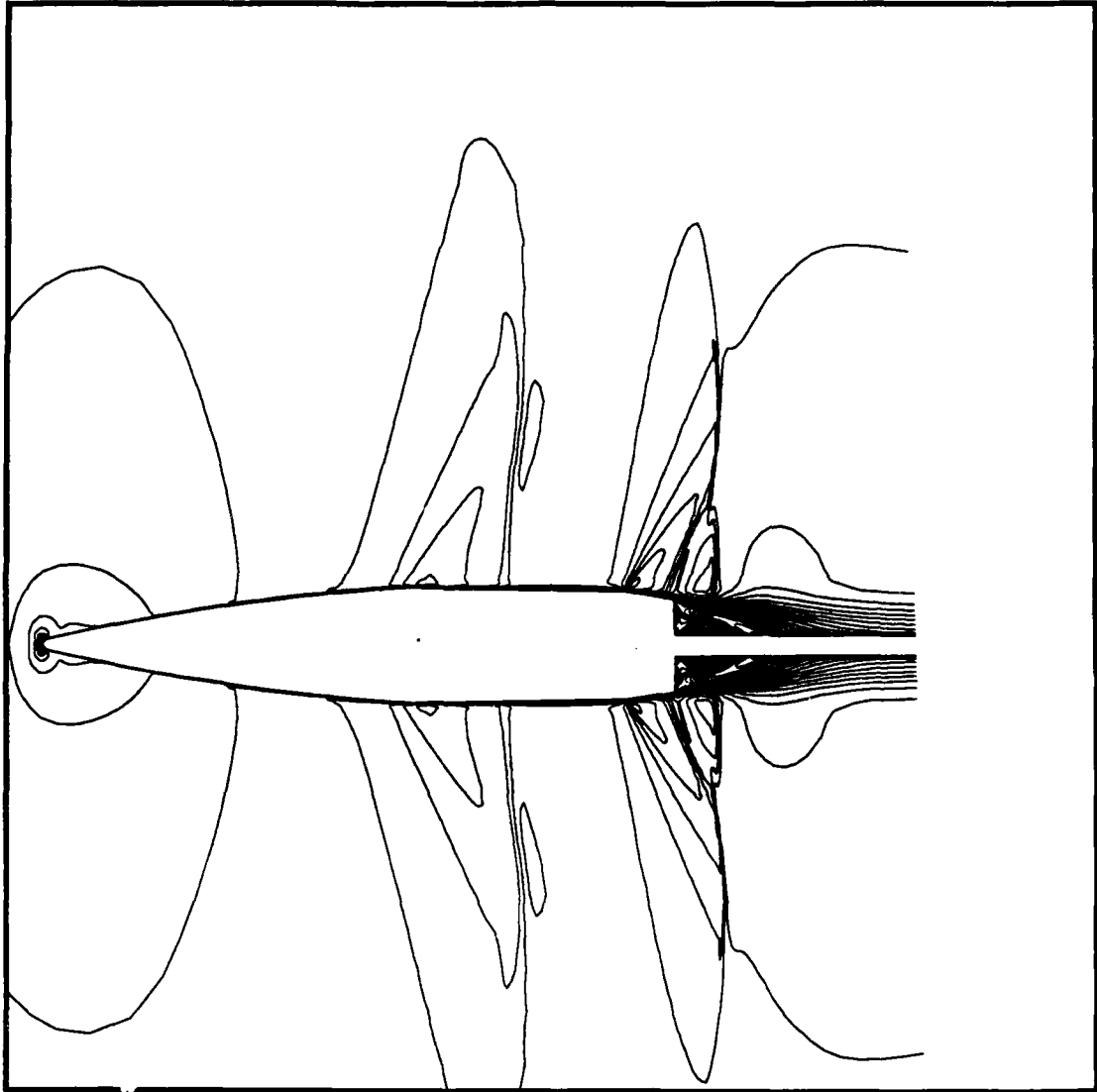


Figure 22. Mach number contours for Mach number 0.97 and  $\alpha = 0.0^\circ$ .

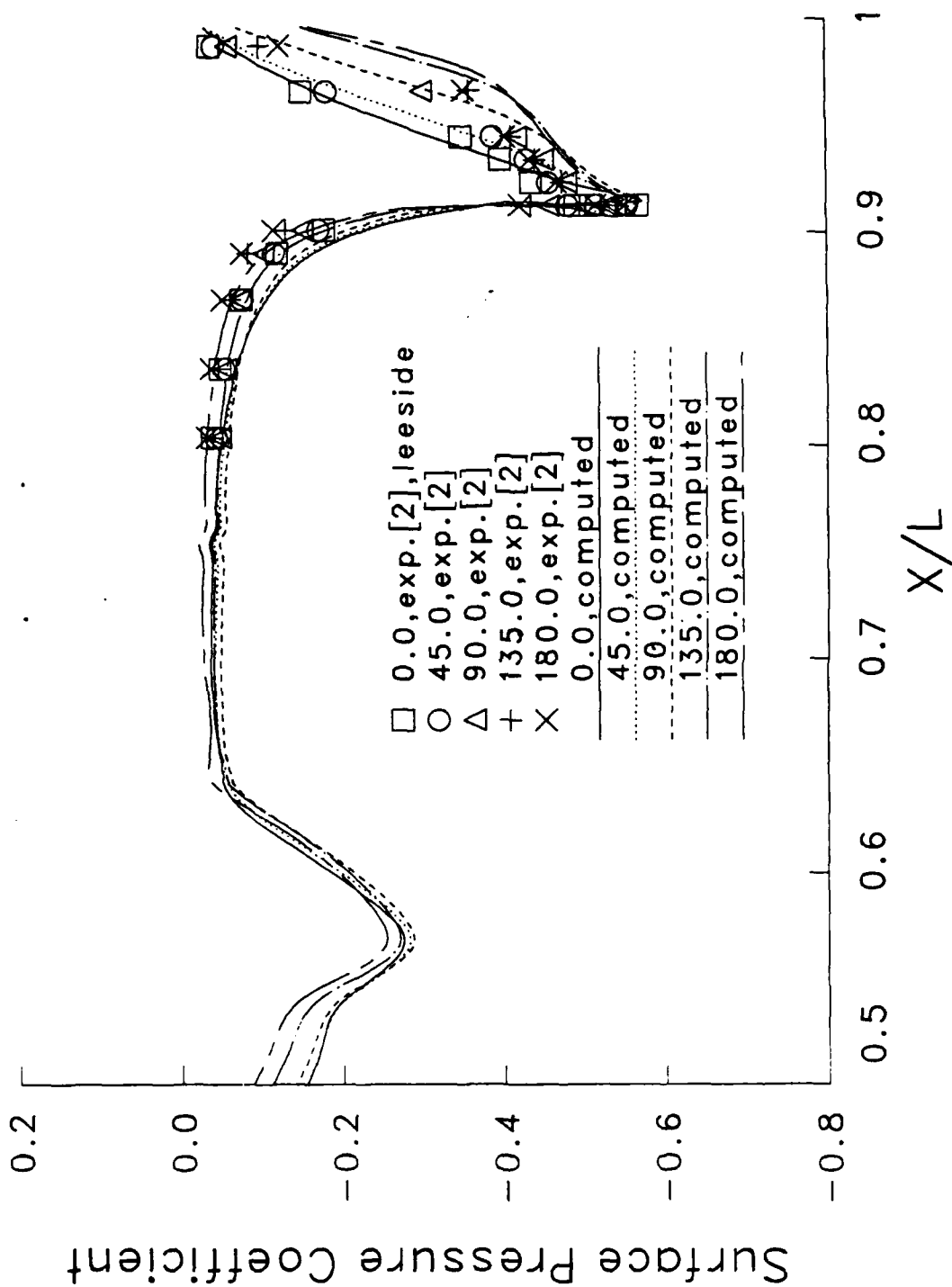


Figure 23. Effect of angle of attack on  $C_p$  and comparison with Danberg's data,  $M_\infty = 0.94$ ,  $\alpha = 4.0^\circ$ ,  $170 \times 50 \times 39$  grid.

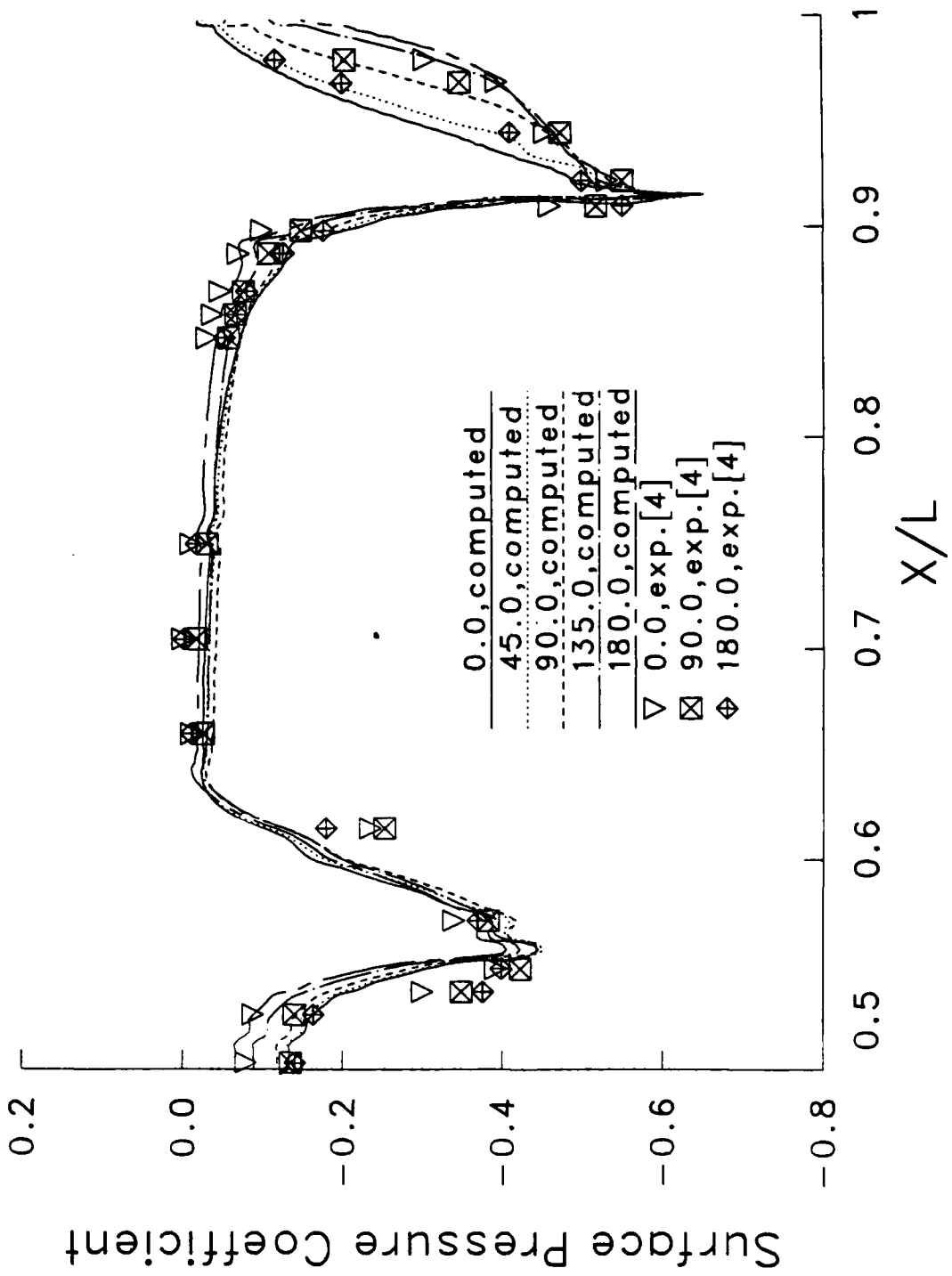


Figure 24. Effect of angle of attack on  $C_p$  and comparison with Miller's data,  $M_\infty = 0.94$ ,  $\alpha = 4.0^\circ$ ,  $170 \times 50 \times 39$  grid.

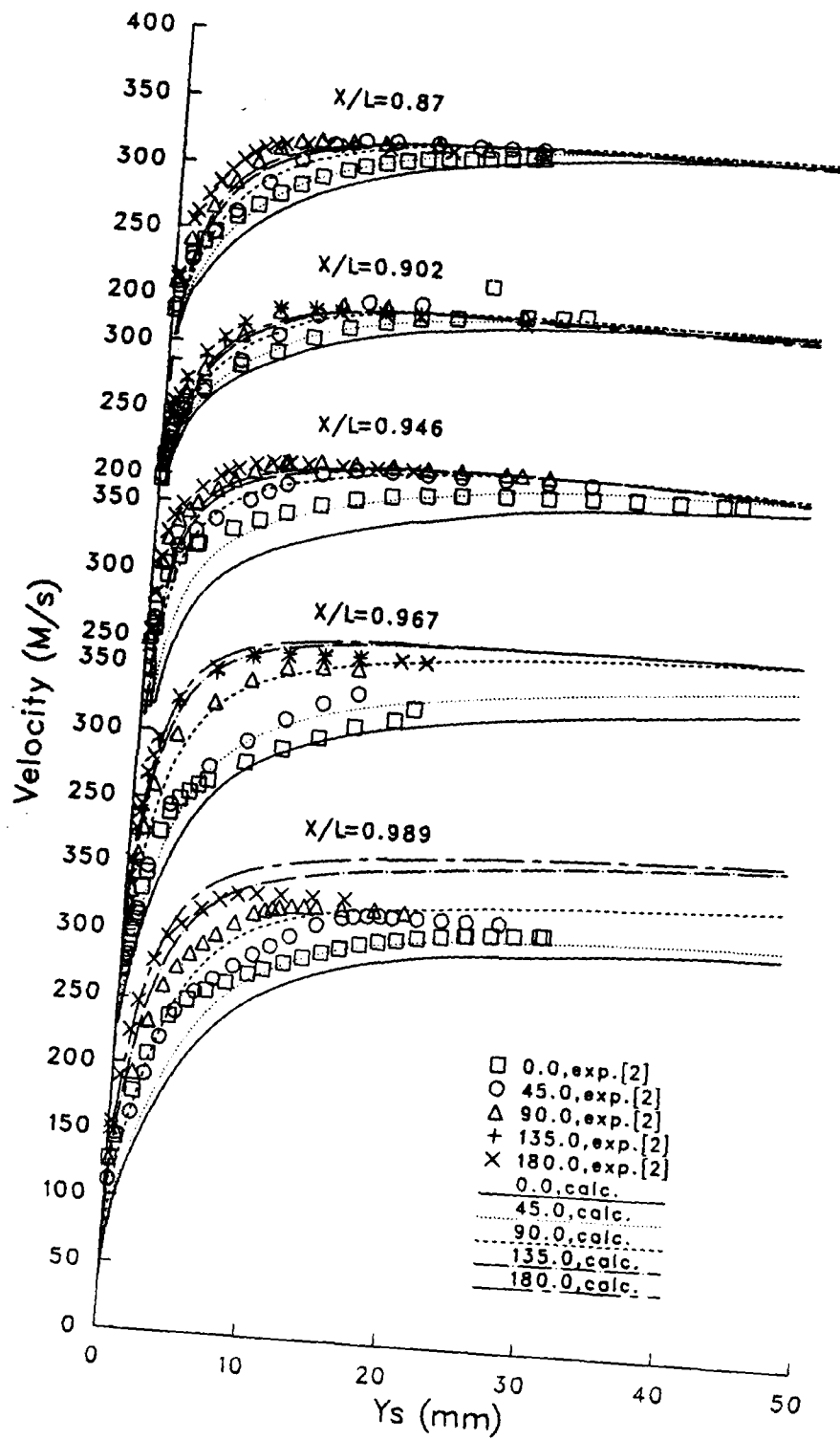


Figure 25. Afterbody velocity profiles at angle of attack using extended boattail grid.

$$M_{\infty} = 0.94, \alpha = 4.0^{\circ}$$

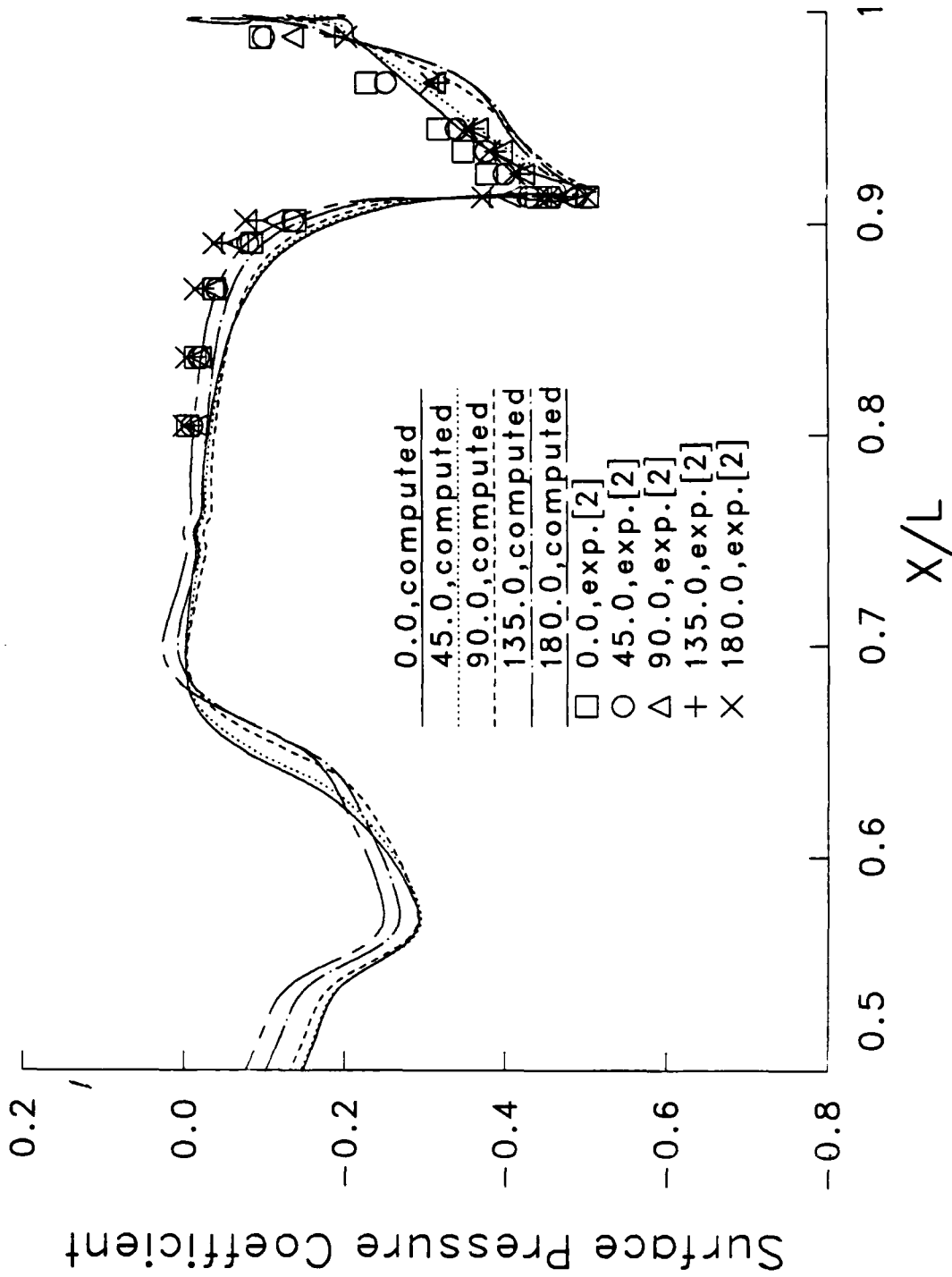


Figure 26. Surface pressure coefficient distributions using wrapped around grid,  $M_\infty = 0.97$ ,  $\alpha = 4.0^\circ$ .

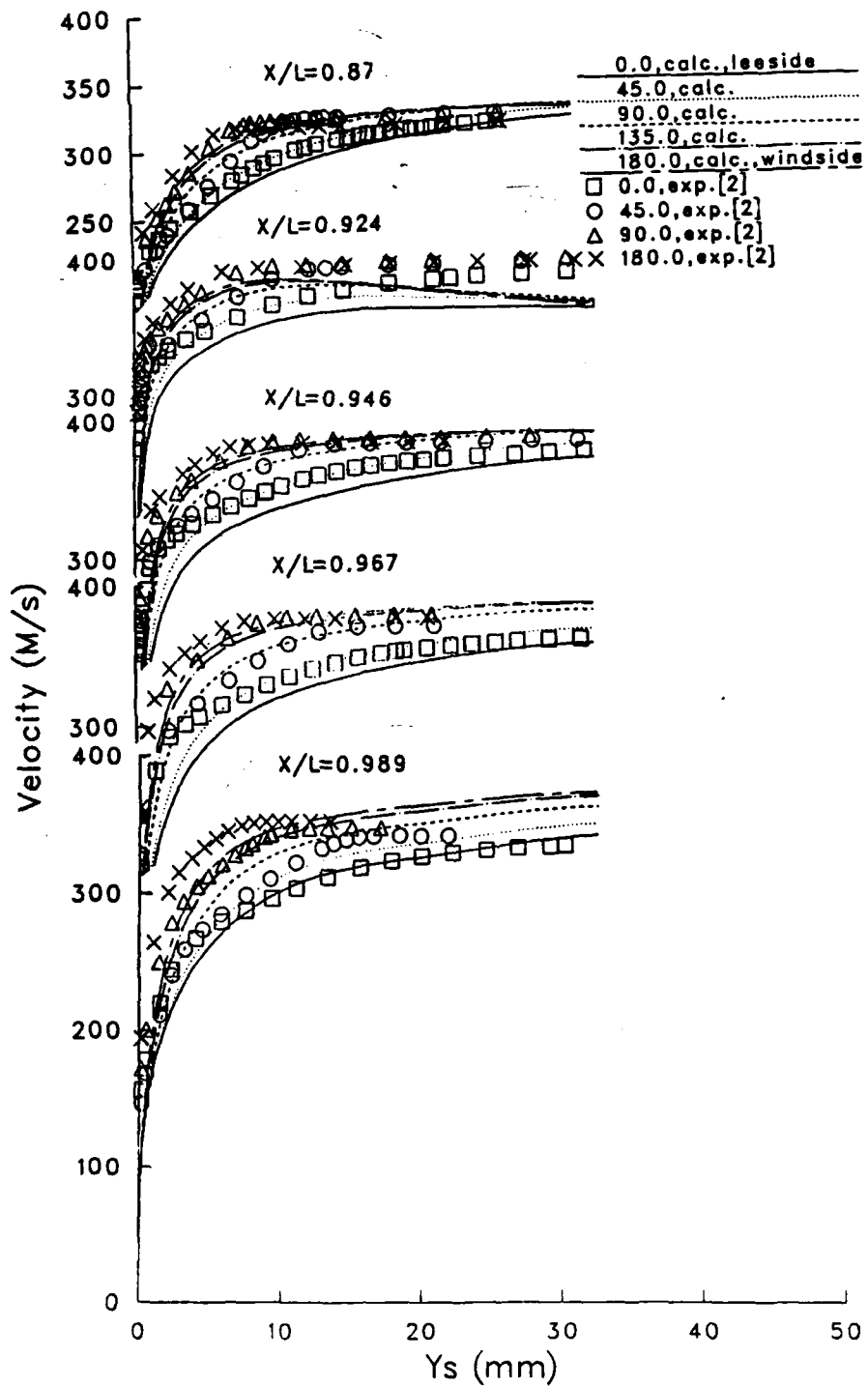


Figure 27. Velocity profiles using wrapped around grid,  $M_\infty = 0.97$ ,  $\alpha = 4.0^\circ$ .

## REFERENCES

1. T.H. Pulliam and J.L. Steger, "On Implicit Finite-Difference Simulations of Three-Dimensional Flow," AIAA Journal Vol. 18, No. 2, February 1980, pp159-167.
2. J.E. Danberg, unpublished wind tunnel data on M549 obtained in the NASA Langley Research Center 8 Foot Transonic Pressure Tunnel, 1978-1979.
3. J.E. Danberg, R.P. Reklis and G.R. Inger, "Pressure Distributions and Boundary Layer Profiles on a Yawed Projectile at Transonic Speed," University of Delaware, Mechanical and Aerospace Engineering Department, Technical Report No. 226, April 1979.
4. M.C. Miller and J.W. Molnar, "Wind Tunnel Measurements of the Induced Surface Pressures on a Spinning Artillery Projectile Model in the Transonic Speed Regime," Chemical Research, Development and Engineering Center, CRDEC-TR-86081, September 1986.
5. L.D. Kayser, "Surface Pressure Measurements on a Projectile Shape at Mach 0.908," U.S. Army Armament Research and Development Command, Ballistic Research Laboratory, ARBRL- MR-03079, Aberdeen Proving Ground, Maryland, February 1981.
6. L.D. Kayser and F. Whiton, "Surface Pressure Measurements on a Boattailed Projectile Shape at Transonic Speeds," U.S. Army Armament Research and Development Command, Ballistic Research Laboratory, ARBRL-MR-03161, Aberdeen Proving Ground, Maryland, March 1982 (AD A113520).
7. J.A. Krupp and E.M. Murman, "Computation of Transonic Flows Past Lifting Airfoils and Slender Bodies," AIAA Journal Vol. 10, July 1972, pp.880-886.
8. J.B. McDivitt and R.A. Taylor, "Pressure Distributions at Transonic Speeds for Slender Bodies Having Various Axial Locations of Maximum Diameter," NACA TN 4280, 1958.
9. R.A. Taylor and J.B. McDivitt, "Pressure Distributions at Transonic Speeds for Parabolic-Arc Bodies of Revolution Having Fineness Ratios of 10, 12, and 14," NACA TN 4234, March 1958.
10. G. Drougge, "An Experimental Investigation of the Interference Between Bodies of Revolution at Transonic Speeds, with Special Reference to the sonic and Supersonic Area Rule," FFA Report 83, Aeronautical Research Institute of Sweden, 1959.
11. W.L. Chow, L.J. Bober, and B.H. Anderson, "Numerical Calculation of Transonic Boattail Flow," NASA TN D-7984, June 1975.
12. G.D. Shrewsbury, "Effect of Boattail Juncture Shape on Pressure Drag Coefficients of Isolated Afterbodies," NASA TM X-1517, 1968.
13. F.R. Bailey, "Numerical Calculations of Transonic Flow about Slender Bodies of Revolution," NASA TN D-6582, December 1971.

14. R.P. Reklis, W.B. Sturek, and F.R. Bailey, "Computation of Transonic Flow Past Projectiles at Angle of Attack," U.S. Army Armament Research and Development Command, Ballistic Research Laboratory, ARBRL-TR-02139, Aberdeen Proving Ground, Maryland, February 1979, also see AIAA Paper No. 78-1182, July 1978.
15. S.S. Stahara, J.P. Elliott, and J.R. Spreiter, "Transonic Flow Past Axisymmetric and Nonaxisymmetric Boattail Projectiles," AIAA Journal, Vol. 20, No. 10, 1982, pp. 1329-1337.
16. R.P. Reklis, J.E. Danberg and G.R. Inger, "Boundary Layer Flows on Transonic Projectiles," AIAA Paper No. 79-1551, 12th Fluid and Plasma Dynamics Conference, Williamsburg, Virginia, 1979.
17. H.A. Dwyer and B.R. Sanders, "Magnus Forces on Spinning Supersonic Cones, Part I, The Boundary Layer," AIAA Journal Vol. 14, April 1976, p 498.
18. R. Beam and R.F. Warming, "An Implicit Factored Scheme for Compressible Navier-Stokes Equations," AIAA Paper No. 77-645, June 1977.
19. B.S. Baldwin and H. Lomax, "Thin Layer Approximation and Algebraic Model for Separated Turbulent Flows," AIAA Paper No. 78-257, January 1978.
20. G.S. Deiwert, "Numerical Simulation of Three-Dimensional Boattail Afterbody Flowfields," AIAA Journal Vol. 19, No. 5, May 1981, pp. 582-588.
21. D.E. Reubush, "Experimental Study of the Effectiveness of Cylindrical Plume Simulators for Predicting Jet-On Boattail Drag at Mach Numbers up to 1.30," NASA TN D-7795, 1974.
22. J.A. Benek, "Separated and Non-Separated Turbulent Flows about Axisymmetric Nozzle Afterbodies, Part I, Detailed Surface Measurements," AEDC-TR-78-49, and "Part II, Detailed Flow Measurements," AEDC-TR-79-22, October 1979.
23. J. Sahu and J.E. Danberg, "Navier-Stokes Computations of Transonic Flows with a Two-Equation Turbulence Model," AIAA Journal Vol. 24, No. 11, November 1986, pp. 1744-1751
24. B.E. Launder and D. Spalding, "Mathematical Models of Turbulence," Academic Press, Orlando, FL, 1972.
25. D.A. Johnson, C.C. Horstman, and W.D. Bachalo, "Comparison Between Experiment and Prediction for a Transonic Turbulent Separated Flow," AIAA Journal, Vol. 20, June 1982, pp. 737-744.
26. C.J. Nietubicz, T.H. Pulliam, and J.L. Steger, "Numerical Solution of the Azimuthal-Invariant Thin-Layer Navier-Stokes Equations," AIAA Journal Vol. 18, No. 12, December 1980, pp. 1411-1412, (also see ARBRL-TR-02227, March 1980, AD 085716).
27. C.J. Nietubicz, G.R. Inger, and J.E. Danberg, "A Theoretical and Experimental Investigation of a Transonic Projectile Flow Field," AIAA Paper No. 82-0101, 20th Aerospace Sciences Meeting, Orlando, Florida, January 1982, (also see ARBRL-MR-03291, July 1983, AD A131938).

28. C.J. Nietubicz, W.B. Sturek, and K.R. Heavey, "Computations of Projectile Magnus Effect at Transonic Velocities," AIAA Journal, Vol. 23, No. 7, July 1985, (also see, ARBRL-TR-02515, August 1983).
29. C.J. Nietubicz, D.C. Mylin, and J. Sahu, "Aerodynamic Coefficient Predictions for a Projectile Configuration at Transonic Speeds," AIAA Paper No. 84-0326, 22nd Aerospace Sciences Meeting, Reno, Nevada, January 1984, (see also BRL-MR-3639, December 1987).
30. J. Sahu and C.J. Nietubicz, "Improved Numerical Prediction of Transonic Flow," U.S. Army Ballistic Research Laboratory, BRL-TR-2784, Aberdeen Proving Ground, Maryland, March 1987.
31. J. Sahu and J.L. Steger, "Numerical Simulation of Three Dimensional Transonic Flows," AIAA Paper No. 87-2293, Atmospheric Flight Mechanics Conference, Monterey, California, August 1987, (also see BRL-TR-2903, March 1988).
32. T.H. Pulliam and J.L. Steger, "Recent Improvements in Efficiency, Accuracy and Convergence of Implicit Approximate Factorization Algorithms," AIAA Paper 85-0360, January 1985.
33. J. Sahu, "Numerical Computations of Transonic Critical Aerodynamic Behavior," Paper 88-4038-CP, AIAA/ASME/SIAM/APS 1st National Fluid Dynamic Conference, Cincinnati, Ohio, July 1988.
34. J.L. Steger, "Implicit Finite-Difference Simulation of Flow about Arbitrary Geometries with Application to Airfoils," AIAA journal, Vol. 16, No. 4, July 1978, pp. 679-686.
35. C. J. Nietubicz, K. R. Heavey, and J. L. Steger, "Grid Generation Technique for Projectile Configurations," ARO Report 82-3, Proceedings of the 1982 Army Numerical Analysis and Computers Conference, August 1982.



## LIST OF SYMBOLS

a	speed of sound
$c_p$	specific heat at constant pressure
$C_p$	pressure coefficient
D	projectile diameter
e	total energy per unit volume
$\hat{E}, \hat{F}, \hat{G}, \hat{H}$	flux vectors in transformed coordinates
J	jacobian
L	length of the body
M	Mach number
$p'_o$	total head or impact pressure
$Pr$	Prandtl number
$Pr_t$	turbulent Prandtl number
$\hat{q}$	vector of dependent variables
r	recovery factor
R	body radius
$\hat{S}$	inviscid source term
t	time
T	temperature
$T_o$	stagnation temperature
u,v,w	axial, circumferential, and normal velocity components of the Navier-Stokes equations
U,V,W	Contravariant velocities of the transformed Navier-Stokes equations
$\bar{V}$	boundary layer velocity parallel to surface
X	distance from projectile nose along the axis of symmetry
$Y_s$	distance normal to the body surface

### Greek Symbols

$\alpha$	Angle of attack
$\gamma$	ratio of specific heats
$\kappa$	molecular and turbulent thermal conductivity
$\mu$	molecular and turbulent viscosity
$\xi, \eta, \zeta$	transformed coordinates
$\rho$	density
$\phi$	circumferential angle

### Subscripts

aw	adiabatic wall conditions
wall	wall conditions
$\infty$	free stream conditions



## APPENDIX

### EXPERIMENTAL DATA FROM NASA LANGLEY RESEARCH CENTER WIND TUNNEL TESTS OF THE M549 MODEL

Two test programs (test 822 in August 1978 and 851 in August 1980) were carried out on a model of the M549 projectile as described in section II. The purpose of this appendix is to document the reduced data from these tests and to describe the data reduction procedure in sufficient detail so that alternate reduction methods can be applied. Figure 3 describes the geometry and dimensions of the wind tunnel model. Table 2 contains the key to the subsequent data tables.

#### 1. DATA REDUCTION

The wall pressure measurements are reported here in terms of a nondimensional pressure coefficient:

$$C_p = 2 \frac{(p_{wall} - p_{\infty})}{\gamma p_{\infty} M_{\infty}^2} \quad (7)$$

and  $p_{\infty}$  is obtained from isentropic flow formulas for the measured stagnation pressure which was nominally 101.5 kPa.

Total head or impact pressures,  $p'_0(y)$ , were measured using a pitot probe attached to the survey mechanism as describe in Figure 4. Mach numbers,  $M(y)$ , were calculated for each pitot measurement assuming a constant static pressure corresponding to the measured wall pressure at that station. The local Mach number was calculated from the ratio,  $p'_0/p_{wall}$  using isentropic equations for  $M \leq 1.0$  and the Rayleigh pitot equation for  $M > 1.0$ .

Velocities were calculated from the following relationship:

$$\bar{V} = \bar{V}_{\infty} \frac{M}{M_{\infty}} \sqrt{\frac{T}{T_{\infty}}} \quad (8)$$

The local temperature is evaluated using the linear Crocco temperature-velocity relationship:

$$\frac{T_0 - T_{aw}}{T_{0\infty} - T_{aw}} = \frac{\bar{V}}{\bar{V}_{\infty}} \quad (9)$$

where the local total temperature in this formula can be related to the local static temperature as follows:

$$\frac{T}{T_{\infty}} = \frac{T_0}{T_{\infty}} - \frac{\gamma - 1}{2} M_{\infty}^2 \left( \frac{\bar{V}}{\bar{V}_{\infty}} \right)^2 \quad (10)$$

The wall temperature, which is assumed to be adiabatic, can be written as :

$$\frac{T_{aw}}{T_{\infty}} = 1 + r \frac{\gamma - 1}{2} M_{\infty}^2 \quad (11)$$

where  $r$  is the recovery factor which is taken as 0.9 in these calculations. The free stream stagnation temperature is:

$$\frac{T_{0\infty}}{T_\infty} = 1 + \frac{\gamma - 1}{2} M_\infty^2 \quad (12)$$

When the five equations, 8 to 12, are combined and solved for the velocity ratio, one obtains:

$$\frac{\bar{V}}{\bar{V}_\infty} = \frac{(\gamma - 1)M^2}{4 + 2(\gamma - 1)M^2} \left[ (1 - r) + \sqrt{(1 - r)^2 + 4 \left( \frac{2}{(\gamma - 1)M^2} + 1 \right) \left( \frac{2}{(\gamma - 1)M_\infty^2} + r \right)} \right] \quad (13)$$

Equation 13 was used to calculate the local velocity after the free stream velocity,  $\bar{V}_\infty$  was calculated from  $M_\infty$  and the free stream stagnation temperature of 322.2 K.

TABLE 2: Directory of Data Tables.

$M_\infty$	$\alpha$	X/L	$\phi$	table	contents
0.94	0.0	all	N/A	2	$C_p$ vs X/L
0.97	0.0	all	N/A	2	" "
0.94	4.0	all	all	3	" "
0.97	4.0	all	all	4	" "
0.94	0.0	all	N/A	5	$V$ (m/s) vs $y$ (mm)
0.94	4.0	0.870	all	6	" " "
0.94	4.0	0.902	all	7	" " "
0.94	4.0	0.924	all	8	" " "
0.94	4.0	0.946	all	9	" " "
0.94	4.0	0.967	all	10	" " "
0.94	4.0	0.989	all	11	" " "
0.97	0.0	all	N/A	12	" " "
0.97	4.0	0.870	all	13	" " "
0.97	4.0	0.924	all	14	" " "
0.97	4.0	0.946	all	15	" " "
0.97	4.0	0.967	all	16	" " "
0.97	4.0	0.989	all	17	" " "

TABLE 3: Pressure Coefficient Data at Zero Angle of Attack

TAP NO.	X/L	$C_p$	
		$M_\infty=0.94$	$M_\infty=0.97$
1	0.805	-0.040	0.000
2	0.837	-0.054	-0.014
3	0.870	-0.068	-0.029
12	0.891	-0.107	-0.063
4	0.902	-0.165	-0.127
5	0.913	-0.535	-0.478
6	0.924	-0.542	-0.478
14	0.935	-0.505	-0.439
7	0.946	-0.472	-0.413
8	0.967	-0.314	-0.345
9	0.989	-0.036	-0.106
10	0.913	-0.523	-0.464
11	0.913	-0.561	-0.497
13	0.913	-0.561	-0.439

TABLE 4: Surface Pressure Coefficient,  $M_\infty = 0.94, \alpha = 4^\circ$

X/L	$C_p$				
	$\phi$				
	0.0	45.0	90.0	135.0	180.0
0.8048	-.039	-.044	-.049	-.040	-.033
0.8372	-.050	-.055	-.057	-.048	-.039
0.8699	-.076	-.077	-.075	-.062	-.052
0.9024	-.179	-.172	-.152	-.131	-.116
0.9132	-.491	-.481	-.458	-.436	-.422
0.9241	-.436	-.457	-.480	-.474	-.467
0.9458	-.349	-.388	-.418	-.411	-.403
0.9675	-.152	-.183	-.301	-.360	-.353
0.9892	-.039	-.044	-.060	-.100	-.125
0.9132	-.510	-.516	-.531	-.542	-.552
0.8916	-.121	-.117	-.104	-.085	-.077
0.9132	-.568	-.555	-.540	-.522	-.516
0.9349	-.398	-.430	-.451	-.441	-.434

TABLE 5: Surface Pressure Coefficient,  $M_\infty = 0.97, \alpha = 4^\circ$

X/L	$C_p$				
	$\phi$				
	0.0	45.0	90.0	135.0	180.0
0.8048	-0.006	-0.011	-0.017	-0.010	-0.001
0.8373	-0.016	-0.020	-0.022	-0.014	-0.005
0.8699	-0.040	-0.043	-0.038	-0.026	-0.016
0.9024	-0.141	-0.138	-0.114	-0.093	-0.079
0.9132	-0.441	-0.431	-0.408	-0.383	-0.374
0.9241	-0.379	-0.401	-0.424	-0.420	-0.413
0.9458	-0.319	-0.342	-0.368	-0.363	-0.355
0.9675	-0.230	-0.254	-0.315	-0.320	-0.311
0.9892	-0.098	-0.102	-0.138	-0.191	-0.205
0.9132	-0.456	-0.461	-0.476	-0.490	-0.503
0.8916	-0.087	-0.082	-0.069	-0.050	-0.040
0.9132	-0.504	-0.490	-0.477	-0.459	-0.456
0.9349	-0.350	-0.378	-0.398	-0.390	-0.383

TABLE 6: Velocity Data at Zero Angle of Attack for Mach Number 0.94

X/L									
0.902		0.924		0.946		0.967		0.989	
y(mm)	V(m/s)								
0.000	0.0	0.000	0.0	0.000	0.0	0.000	0.0	0.000	0.0
0.147	197.3	0.147	229.3	0.168	240.5	0.145	159.6	0.161	111.6
0.262	218.8	0.147	229.6	0.207	240.5	0.152	160.2	0.188	112.2
0.404	228.4	0.330	271.0	0.557	291.6	0.292	173.7	0.626	140.0
0.518	230.9	0.434	287.7	1.196	319.7	0.401	179.4	1.070	162.9
0.658	234.7	0.564	298.2	1.824	330.5	0.513	189.0	1.522	184.2
0.787	244.1	0.688	302.6	3.138	342.1	0.909	219.6	1.963	204.9
0.919	248.5	0.912	311.7	4.316	350.6	1.112	253.3	2.885	235.6
1.201	253.1	1.476	320.7	5.600	358.2	2.682	303.1	3.803	252.7
1.392	257.1	2.055	327.4	6.772	364.5	5.194	313.6	4.605	262.2
2.106	268.1	2.715	334.3	8.120	371.0	6.452	323.2	5.484	270.5
2.741	274.7	3.942	344.3	9.265	375.6	8.966	339.1	6.321	276.8
3.371	281.3	5.205	352.0	9.957	377.8	10.218	345.3	6.351	277.5
3.807	287.8	7.739	366.0	10.610	379.4	12.779	351.4	7.244	284.1
4.559	294.3	10.373	374.9	11.807	381.0	15.268	352.5	8.088	289.7
5.215	299.8	12.756	376.9	13.009	382.0	18.097	352.7	8.936	295.7
7.775	318.3	15.331	377.2	14.274	382.3	19.322	352.7	9.910	301.6
10.277	330.8	17.790	378.4	15.575	382.4			10.677	305.9
12.850	333.0	20.406	380.2	16.814	382.5			11.670	310.6
15.380	333.3	23.322	381.2	19.329	382.6			12.805	314.4
17.950	333.5	28.733	381.4	21.823	382.6			12.858	314.3
20.551	333.5	28.860	381.9	21.859	382.8			14.234	316.8
				26.908	382.9			15.605	317.7
				31.947	382.9			16.942	318.0
								18.267	318.0
								19.578	318.0
								21.969	318.0
								24.216	317.9
								25.865	318.0

TABLE 7: Velocity Data at Four Degrees Angle of Attack for Mach Number 0.94

X/L= 0.870

$\phi$							
$0^\circ$		$45.0^\circ$		$90.0^\circ$		$180.0^\circ$	
y(mm)	V(m/s)	y(mm)	V(m/s)	y(mm)	V(m/s)	y(mm)	V(m/s)
0.000	0.0	0.000	0.0	0.000	0.0	0.000	0.0
0.192	187.2	0.207	190.4	0.161	208.6	0.195	210.5
0.197	187.1	0.211	190.4	0.198	211.4	0.208	213.7
1.170	229.7	1.143	226.2	0.978	241.6	1.084	255.3
1.908	240.7	2.570	247.5	2.437	267.4	1.361	261.9
2.634	248.1	4.050	264.1	3.936	286.4	2.091	275.0
4.165	260.1	6.289	286.5	5.400	302.0	2.821	285.3
5.610	269.8	8.482	305.3	6.890	313.9	2.867	286.0
7.114	279.1	10.750	318.6	8.326	319.4	3.556	294.7
8.564	286.5	12.972	322.5	9.806	320.9	4.375	303.2
10.054	293.3	15.251	322.9	12.078	321.4	5.051	308.8
11.807	299.7	18.264	323.2	14.421	321.6	5.769	313.0
13.050	303.5	21.240	323.4	18.254	322.0	5.779	313.0
14.561	306.8	21.258	323.5	21.861	322.3	6.521	315.5
14.561	306.7	23.529	323.5	25.639	322.6	7.264	316.7
16.079	309.3	25.858	323.7			8.802	317.7
17.510	311.2					10.288	317.8
17.534	311.0					11.761	317.9
19.076	312.7					14.804	318.1
20.676	314.2					19.361	318.3
22.077	315.3					26.032	318.6
23.617	316.3						
25.168	317.4						
25.897	318.0						

TABLE 8: Velocity Data at Four Degrees Angle of Attack for Mach Number 0.94

X/L= 0.902

		$\phi$							
$0^\circ$		$45.0^\circ$		$90.0^\circ$		$135.0^\circ$		$180.0^\circ$	
y(mm)	V(m/s)	y(mm)	V(m/s)	y(mm)	V(m/s)	y(mm)	V(m/s)	y(mm)	V(m/s)
0.000	0.0	0.000	0.0	0.000	0.0	0.000	0.0	0.000	0.0
0.147	195.0	0.150	197.3	0.145	207.2	0.147	209.8	0.145	206.6
0.267	213.3	0.274	209.7	0.269	214.6	0.287	215.9	0.272	213.1
0.419	221.0	0.432	215.5	0.432	222.3	0.409	227.1	0.396	223.7
0.579	225.1	0.650	230.9	0.643	240.4	0.536	244.2	0.539	248.6
0.653	235.3	0.937	238.8	0.909	248.8	0.688	250.4	0.688	252.6
0.902	247.8	1.168	241.0	1.412	261.1	1.031	256.3	1.008	257.5
1.161	246.6	1.402	247.5	2.636	279.6	1.481	269.1	1.448	271.8
1.417	253.4	2.692	262.6	5.222	306.8	2.703	289.1	2.700	292.0
2.703	265.4	5.232	287.2	7.760	325.9	3.960	301.3	3.960	304.5
5.199	284.0	7.793	308.1	10.279	355.8	5.243	314.2	5.321	316.5
7.772	295.6	10.490	325.0	12.261	334.2	7.793	328.7	7.767	327.6
10.305	308.1	14.079	336.8	15.425	334.5	10.312	330.4	10.307	328.7
12.830	317.2	17.902	337.6	25.349	334.7	12.164	330.6	12.126	328.7
15.438	323.0					15.367	330.9	15.329	329.0
17.915	327.2					17.869	330.9	17.864	329.0
20.536	330.3					25.207	331.5	25.425	329.3
22.913	355.6								
25.529	334.4								
28.070	335.7								
29.756	337.6								

TABLE 9: Velocity Data at Four Degrees Angle of Attack for Mach Number 0.94

X/L= 0.924

$\phi$							
$0^\circ$		$90.0^\circ$		$135.0^\circ$		$180.0^\circ$	
y(mm)	V(m/s)	y(mm)	V(m/s)	y(mm)	V(m/s)	y(mm)	V(m/s)
0.000	0.0	0.000	0.0	0.000	0.0	0.000	0.0
0.140	212.7	0.147	230.3	0.150	242.1	0.147	239.6
0.147	213.6	0.150	240.2	0.165	250.3	0.163	242.1
0.279	236.6	0.292	270.9	0.279	268.0	0.269	266.1
0.401	260.5	0.480	288.5	0.406	281.8	0.399	283.8
0.559	273.8	0.541	296.4	0.518	300.0	0.513	303.6
0.663	281.6	0.798	310.5	0.658	312.3	0.660	315.3
0.780	290.4	0.907	314.1	0.818	318.7	0.803	321.2
0.916	294.2	1.181	318.9	0.899	320.7	0.912	324.0
1.044	296.9	1.453	324.5	1.161	325.7	1.148	329.0
1.290	300.6	2.060	332.8	1.344	330.7	1.410	334.2
1.669	306.6	2.662	338.8	2.075	340.7	2.055	343.4
2.024	309.2	3.942	349.5	2.652	346.6	2.657	350.3
2.644	314.6	5.161	358.4	3.957	356.9	3.922	359.8
3.909	323.0	7.752	372.5	5.128	365.2	5.253	368.5
5.154	329.1	10.234	378.3	7.739	376.2	7.704	376.1
7.673	340.3	12.891	378.8	10.213	377.9	10.213	377.1
10.251	349.4	15.207	379.3	12.797	378.2	12.736	377.4
12.725	355.5	17.755	380.8	12.822	378.2	12.896	37.4
15.230	359.9	20.351	381.8	15.197	379.2	15.207	378.4
17.732	364.3	23.373	382.8	17.838	380.4	17.808	379.4
20.424	368.4	26.086	383.3	20.330	381.6	20.383	380.4
23.145	370.4	28.618	384.3	23.411	382.4	23.368	381.9
26.032	372.2			25.956	382.9	26.137	382.6
28.763	375.0			27.894	383.4	27.838	382.6
				28.616	383.6	28.689	382.6

TABLE 10: Velocity Data at Four Degrees Angle of Attack for Mach Number 0.94

X/L= 0.946

$\phi$							
$0^\circ$		$45.0^\circ$		$90.0^\circ$		$180.0^\circ$	
y(mm)	V(m/s)	y(mm)	V(m/s)	y(mm)	V(m/s)	y(mm)	V(m/s)
0.000	0.0	0.000	0.0	0.000	0.0	0.000	0.0
0.145	201.6	0.178	233.3	0.184	248.3	0.189	254.0
0.215	213.0	0.185	233.8	0.200	251.0	0.197	252.5
0.270	225.8	0.404	262.8	0.266	262.9	0.357	281.0
0.523	255.8	1.039	303.8	0.394	279.3	0.583	307.7
0.546	258.4	1.674	316.6	0.706	304.1	0.930	326.5
1.143	295.1	2.898	329.1	1.026	322.2	1.269	338.6
1.875	309.5	4.225	338.7	1.649	336.2	1.830	347.7
3.014	319.0	6.602	353.9	2.265	343.8	3.113	361.0
3.185	320.0	7.915	361.0	2.811	349.2	4.357	370.3
5.519	332.2	9.182	367.3	2.881	350.0	4.946	373.8
7.358	339.6	11.670	377.0	4.208	360.4	5.634	377.1
9.297	346.3	14.101	381.1	5.406	368.1	6.848	380.9
11.746	353.9	14.160	381.2	6.785	375.5	8.090	382.6
14.228	359.6	16.673	381.8	7.949	380.6	9.251	383.0
16.792	363.7	19.227	382.1	8.993	383.4	9.318	383.0
19.323	366.6	21.709	382.1	9.168	383.8	10.636	383.2
21.766	368.4	24.905	382.1	11.555	385.6	13.090	383.4
21.840	368.3	28.006	382.3	14.025	386.1	15.578	383.6
25.008	369.9	31.131	382.2	16.742	386.1	18.166	383.5
28.098	371.2			19.237	386.2		
31.250	372.4			21.637	386.3		
34.426	373.5			24.892	386.4		
37.520	374.3			26.048	386.4		
40.676	374.9			28.032	386.4		
41.986	374.9						

TABLE 11: Velocity Data at Four Degrees Angle of Attack for Mach Number 0.94

X/L= 0.967

		$\phi$							
$0^\circ$		$45.0^\circ$		$90.0^\circ$		$135.0^\circ$		$180.0^\circ$	
y(mm)	V(m/s)	y(mm)	V(m/s)	y(mm)	V(m/s)	y(mm)	V(m/s)	y(mm)	V(m/s)
0.000	0.0	0.000	0.0	0.000	0.0	0.000	0.0	0.000	0.0
0.152	120.0	0.155	120.9	0.152	162.9	0.152	188.2	0.152	189.9
0.160	121.7	0.279	127.2	0.285	171.0	0.287	198.7	0.274	201.7
0.287	128.6	0.406	132.0	0.406	180.0	0.409	220.8	0.406	225.9
0.414	135.2	0.648	150.5	0.655	207.3	0.678	240.1	0.546	237.6
0.526	139.6	0.919	166.1	0.897	227.2	0.927	264.5	0.671	243.6
0.650	150.2	1.402	198.6	1.392	259.4	1.430	291.7	0.904	267.3
0.785	158.4	2.664	245.6	2.692	297.9	2.697	322.0	1.158	280.2
0.909	162.8	5.215	275.6	5.215	323.2	5.205	344.9	1.407	294.4
1.156	182.6	7.709	296.3	7.704	341.5	7.716	358.9	2.664	324.8
1.402	194.1	10.320	314.4	10.213	352.7	10.262	363.0	5.161	348.2
2.088	225.6	12.889	328.0	12.736	355.1	12.741	363.8	7.696	359.8
2.670	240.1	15.377	336.8	15.273	355.3	15.281	364.1	10.241	362.1
3.294	250.4					20.069	385.1	12.728	362.9
3.934	256.0							15.276	363.4
4.554	261.5							18.278	363.9
5.192	265.5							20.104	364.2
7.711	280.5								
10.221	292.6								
12.756	302.8								
15.273	312.5								
18.110	319.3								

TABLE 12: Velocity Data at Four Degrees Angle of Attack for Mach Number 0.94

X/L= 0.989

$\phi$							
$0^\circ$		$45.0^\circ$		$90.0^\circ$		$180.0^\circ$	
y(mm)	V(m/s)	y(mm)	V(m/s)	y(mm)	V(m/s)	y(mm)	V(m/s)
0.000	0.0	0.000	0.0	0.000	0.0	0.000	0.0
0.168	126.9	0.169	110.8	0.179	126.0	0.181	154.5
0.178	127.4	0.174	111.2	0.190	127.0	0.181	149.6
0.546	143.9	1.448	162.5	0.543	147.1	0.559	189.3
1.493	179.0	2.239	192.6	1.409	192.6	1.052	223.6
2.360	207.8	3.120	220.5	2.265	231.9	1.477	245.5
3.715	236.6	4.123	240.4	2.287	232.6	2.355	277.4
4.932	249.1	5.397	255.4	3.142	258.8	2.363	277.6
4.952	249.1	6.640	265.6	3.994	273.7	3.264	295.4
6.202	257.0	8.014	276.6	4.890	284.0	4.144	305.3
7.567	263.9	9.367	286.0	5.788	292.4	5.480	317.4
9.115	271.3	10.571	293.6	6.667	299.3	6.775	325.3
10.166	275.9	11.929	301.8	6.681	299.7	8.068	329.8
11.617	281.7	13.769	311.5	7.926	308.8	9.393	331.3
12.922	286.6	15.573	317.7	9.256	316.8	11.121	331.6
14.256	291.0	16.395	319.3	10.054	319.6	13.384	331.5
15.513	294.7	17.376	320.3	10.570	321.7	15.671	331.4
15.555	295.2	18.274	320.8	11.062	322.7		
16.950	298.9	19.177	321.0	11.931	324.2		
18.270	301.9	20.939	321.1	12.823	324.5		
19.578	304.4	22.719	321.1	13.708	325.0		
21.080	306.9	24.495	321.1	15.509	324.6		
22.776	309.0	26.895	321.0	17.861	324.9		
				20.014	325.0		

TABLE 13: Velocity Data for Zero Angle of Attack for Mach Number 0.97

X/L									
0.870		0.924		0.946		0.967		0.989	
y(mm)	V(m/s)								
0.000	0.0	0.000	0.0	0.000	0.0	0.000	0.0	0.000	0.0
0.186	192.5	0.174	276.8	0.175	231.9	0.177	220.9	0.169	150.8
0.661	221.6	0.413	313.0	0.207	237.9	0.843	277.0	0.180	152.2
1.380	237.5	0.743	327.1	0.323	260.1	1.373	299.2	0.618	188.1
2.147	249.6	1.272	336.7	0.440	275.1	2.287	319.3	1.552	234.5
2.839	258.6	1.287	337.0	0.565	287.2	3.472	330.2	2.468	263.0
4.333	276.8	2.673	350.6	1.188	317.7	4.548	338.1	3.222	276.6
5.820	293.2	3.822	359.6	1.812	327.6	5.612	345.2	4.053	286.1
7.277	307.2	4.973	367.2	2.494	334.2	6.671	352.1	5.085	294.9
7.295	307.1	6.192	374.9	3.013	338.5	7.740	358.5	5.970	301.8
8.787	316.7	6.192	374.8	3.111	339.6	7.784	358.5	6.827	308.4
10.291	321.0	7.362	381.5	4.242	348.3	8.834	364.4	7.530	313.4
11.699	322.0	8.740	387.4	5.569	357.0	9.886	369.0	8.458	320.2
13.253	322.1	9.862	390.8	6.854	365.2	10.950	372.4	9.339	325.5
14.016	322.4	11.055	392.4	8.041	371.7	11.475	373.6	10.289	331.0
15.546	322.4	12.941	393.5	9.273	377.2	11.977	374.4	11.200	334.9
15.556	322.5	14.837	394.4	9.386	377.6	12.493	375.0	12.050	337.7
18.531	322.6	16.102	395.0	11.764	382.8	13.126	375.6	12.934	339.6
22.383	322.8	17.964	395.6	14.247	383.6	14.162	375.9	13.780	340.4
26.175	323.0	21.072	396.2	16.834	383.9	15.237	376.1	14.246	340.7
		24.281	396.7	19.337	383.8	16.336	376.0	15.556	340.8
		27.448	396.9	21.882	383.9	18.514	376.0	17.456	341.0
		27.468	396.8	25.051	384.1	23.903	376.0	19.151	340.8
		30.643	397.0	28.140	383.9	29.458	376.0		
		33.813	397.1	31.308	383.9	32.590	376.0		
		36.999	397.1						
		40.175	397.1						
		43.571	397.1						
		44.108	397.1						

TABLE 14: Velocity Data at Four Degrees Angle of Attack for Mach Number 0.97

X/L= 0.870

$\phi$							
$0^\circ$		$45.0^\circ$		$90.0^\circ$		$180.0^\circ$	
y(mm)	V(m/s)	y(mm)	V(m/s)	y(mm)	V(m/s)	y(mm)	V(m/s)
0.000	0.0	0.000	0.0	0.000	0.0	0.000	0.0
0.141	188.3	0.179	189.6	0.161	205.5	0.186	208.5
0.174	190.7	0.179	189.4	0.188	208.9	0.196	206.9
1.165	227.3	0.857	213.8	0.926	236.2	0.758	241.6
1.899	236.8	1.623	227.9	1.766	252.6	1.464	258.8
2.688	245.0	2.486	240.0	2.403	262.5	2.909	283.4
4.099	257.1	3.952	258.2	3.046	272.0	4.287	301.4
5.581	268.6	5.388	275.2	3.999	285.2	5.801	314.1
5.595	268.8	6.993	293.3	5.486	304.0	7.392	318.1
7.075	278.8	8.517	308.5	6.929	316.6	8.094	317.8
7.758	283.2	9.294	314.2	6.942	316.7	8.842	318.5
8.599	288.2	9.997	319.0	7.960	321.1	10.369	318.1
9.316	291.6	10.799	322.3	8.429	322.1	11.847	318.1
10.089	295.3	11.522	323.7	9.165	322.8	13.304	318.5
11.585	301.2	12.264	324.6	9.863	323.2	14.838	318.4
12.253	302.9	13.063	325.0			14.843	318.4
13.066	305.2					18.769	318.6
14.581	308.5					22.386	318.7
15.321	309.8					26.131	319.1
16.137	311.3						
16.807	312.3						
17.573	312.9						
18.352	314.1						
19.161	314.9						
19.844	315.8						
20.625	316.1						
21.299	316.9						
22.049	317.2						
22.129	317.4						
23.683	318.5						
25.192	319.6						
25.912	319.9						

TABLE 15: Velocity Data at Four Degrees Angle of Attack for Mach Number 0.97

X/L= 0.924

$\phi$							
$0^\circ$		$45.0^\circ$		$90.0^\circ$		$180.0^\circ$	
y(mm)	V(m/s)	y(mm)	V(m/s)	y(mm)	V(m/s)	y(mm)	V(m/s)
0.000	0.0	0.000	0.0	0.000	0.0	0.000	0.0
0.186	259.3	0.165	269.8	0.167	291.6	0.176	288.9
0.193	261.7	0.211	279.1	0.197	296.1	0.195	289.2
0.334	287.7	0.443	307.3	0.380	319.7	0.263	303.5
0.444	302.5	0.591	314.6	0.547	329.7	0.320	316.1
0.566	309.5	2.425	338.5	0.695	333.4	0.385	324.3
1.231	324.1	4.782	356.8	0.900	338.2	0.442	330.3
1.749	329.6	7.260	372.9	1.022	340.6	0.442	329.2
2.351	334.1	9.736	385.7	1.148	343.0	0.742	342.5
2.392	334.5	12.327	392.7	1.715	350.8	1.331	354.4
3.652	342.3	13.541	393.6	2.351	357.4	2.542	368.4
4.963	348.5	14.699	394.4	2.385	357.5	2.553	368.4
7.284	358.4	14.707	394.4	3.549	367.8	3.794	378.5
9.745	367.2	17.998	395.7	4.765	376.7	6.205	391.3
12.246	373.4	21.142	396.5	7.223	390.5	8.749	393.9
14.747	378.1	27.306	397.0	9.753	395.5	11.827	394.4
14.747	377.9	27.330	397.3	12.128	396.2	14.920	395.8
18.003	382.5	33.667	397.4	14.698	397.4	18.082	396.9
21.100	385.1	40.159	397.3	17.825	398.6	21.183	397.4
22.339	385.7	43.950	397.2	20.988	399.2	24.247	397.8
24.188	387.1			27.294	399.8	27.520	397.8
27.331	388.5			30.433	400.0	27.937	397.9
30.505	389.9			33.667	400.0	31.078	398.1
33.764	390.2			40.070	400.0		
37.014	391.7			43.958	399.9		
40.188	392.3						
42.003	392.2						
44.023	392.5						

TABLE 16: Velocity Data at Four Degrees Angle of Attack for Mach Number 0.97

X/L= 0.946

$\phi$							
$0^\circ$		$45.0^\circ$		$90.0^\circ$		$180.0^\circ$	
y(mm)	V(m/s)	y(mm)	V(m/s)	y(mm)	V(m/s)	y(mm)	V(m/s)
0.000	0.0	0.000	0.0	0.000	0.0	0.000	0.0
0.178	223.4	0.182	236.2	0.151	253.4	0.162	259.3
0.182	223.8	0.182	233.9	0.194	259.5	0.197	258.0
0.232	231.6	0.358	256.3	0.303	271.9	0.536	306.9
0.287	241.6	0.373	258.3	0.915	317.3	1.167	335.5
0.349	248.8	1.016	298.9	1.535	332.2	1.783	345.6
0.408	252.8	1.577	311.0	2.997	348.7	3.405	361.9
0.735	278.2	2.970	324.8	4.000	357.5	4.283	368.9
1.031	293.9	4.007	333.5	6.018	371.3	5.563	376.6
1.655	308.3	5.490	343.9	7.963	381.6	6.739	381.0
2.290	314.6	7.189	355.7	9.711	385.3	8.040	382.7
2.926	319.1	9.038	366.8	11.604	386.4	9.439	383.3
4.088	326.0	9.097	366.9	13.958	386.5	11.798	383.5
5.478	332.7	11.569	378.4	16.576	386.8	14.183	383.6
6.770	338.5	14.063	382.6	19.048	386.7	16.715	383.7
8.028	344.0	16.540	382.9	21.581	386.9	19.304	383.6
9.146	348.5	19.177	383.1	24.804	387.1	21.826	383.9
9.225	348.8	21.600	383.3	27.858	386.9		
10.312	352.7	24.784	383.3				
11.791	357.4	28.074	383.4				
12.911	360.2	31.278	383.3				
14.176	362.9						
15.485	365.4						
16.622	366.8						
17.928	368.3						
19.199	369.5						
20.385	370.5						
21.709	371.3						
21.815	371.5						
24.181	372.6						
26.813	373.7						
29.263	374.8						
31.726	375.8						
34.370	376.6						
36.981	377.1						
39.496	377.9						
41.934	378.2						

TABLE 17: Velocity Data at Four Degrees Angle of Attack for Mach Number 0.97

X/L= 0.967

$\phi$							
$0^\circ$		$45.0^\circ$		$90.0^\circ$		$180.0^\circ$	
y(mm)	V(m/s)	y(mm)	V(m/s)	y(mm)	V(m/s)	y(mm)	V(m/s)
0.000	0.0	0.000	0.0	0.000	0.0	0.000	0.0
0.210	197.8	0.194	203.7	0.187	235.5	0.187	235.1
0.213	197.3	0.207	207.1	0.207	237.5	0.234	241.9
1.319	268.2	2.274	297.4	2.228	327.6	0.816	296.9
2.386	292.7	4.419	316.8	4.356	348.0	1.366	320.4
3.471	301.6	6.628	332.9	6.528	363.5	2.413	341.7
4.494	307.2	8.692	346.5	8.609	373.7	3.488	352.5
6.124	315.4	10.810	358.6	10.720	377.7	4.575	361.1
7.740	322.8	12.963	366.9	12.840	378.0	6.141	370.6
9.295	329.6	15.729	370.4	15.565	378.3	7.700	375.0
10.873	335.2	18.391	370.5	18.291	378.2	7.744	375.1
12.533	340.5	21.138	370.5	20.947	378.4	9.866	376.4
14.129	344.8					12.034	376.5
15.741	348.3					14.159	376.5
17.349	351.1					18.453	376.6
18.423	352.5					20.680	376.5
18.997	353.0						
20.589	354.6						
22.310	356.0						
23.809	357.0						
23.887	356.9						
25.474	357.8						
27.047	358.7						
29.295	359.6						
31.546	360.1						
33.623	360.9						
34.718	361.4						

TABLE 18: Velocity Data at Four Degrees Angle of Attack for Mach Number 0.97

X/L= 0.989

$\phi$							
$0^\circ$		$45.0^\circ$		$90.0^\circ$		$180.0^\circ$	
y(mm)	V(m/s)	y(mm)	V(m/s)	y(mm)	V(m/s)	y(mm)	V(m/s)
0.000	0.0	0.000	0.0	0.000	0.0	0.000	0.0
0.168	155.2	0.176	146.3	0.171	172.1	0.169	193.4
0.179	156.8	0.184	147.3	0.171	172.0	0.180	194.5
0.535	178.4	0.535	168.3	0.520	200.4	1.040	264.4
1.502	219.7	1.480	211.5	1.445	249.9	2.048	300.8
2.328	244.6	2.342	240.4	2.326	279.1	2.774	315.3
4.008	267.7	3.243	259.5	3.115	294.3	3.700	325.9
5.846	280.0	4.482	274.3	4.066	305.7	4.562	334.0
7.497	287.8	5.764	285.3	4.871	313.0	5.381	340.4
7.538	288.2	7.530	299.0	5.831	321.4	6.225	345.7
9.358	296.8	9.243	311.0	6.717	328.3	7.167	349.7
11.084	304.2	11.024	323.0	7.481	333.8	8.031	351.7
13.297	312.4	12.854	333.3	7.963	336.7	8.885	352.6
15.598	319.3	13.700	337.0	8.816	341.6	9.759	352.9
15.612	319.2	14.586	339.8	9.224	343.3	10.667	353.0
17.822	324.1	14.622	339.8	9.302	343.7	12.006	353.0
19.955	327.6	15.515	341.5	10.668	347.0	13.464	352.9
22.162	330.2	16.539	342.2	11.974	348.2		
24.551	332.2	18.400	342.7	13.249	348.5		
26.775	333.6	19.913	342.5	14.957	348.5		
29.076	334.7	21.853	342.6	17.031	348.4		
30.126	335.4						



## DISTRIBUTION LIST

<u>No.</u> <u>Copies</u>	<u>Organization</u>	<u>No.</u> <u>Copies</u>	<u>Organization</u>
12	Administrator Defense Technical Information Center ATTN: DTIC-DDA Cameron Station Alexandria, VA 22304-6145	1	Commander US Army Aviation Systems Command ATTN: AMSAV-DACL 4300 Goodfellow Blvd St Louis, MO 63120-1789
1	HQDA (SARD-TR) Washington, DC 20310	1	Director US Army Aviation Research and Technology Activity Moffett Field, CA 94035-1099
1	Commander US Army Material Command ATTN: AMCDRA-ST 5001 Eisenhower Avenue Alexandria, VA 22333-0001	1	Commander US Army Communications Electronics Command ATTN: AMSEL-ED Fort Monmouth, NJ 07703-5301
1	Commander Armament R&D Center US Army AMCCOM ATTN: SMCAR-MSI Picatinny Arsenal, NJ 07806-5000	2	Commander US Army Missile Command ATTN: AMSMI-RD B. Walker Redstone Arsenal, AL 35898-5000
1	Commander Armament R&D Center US Army AMCCom ATTN: SMCAR-TDC Picatinny Arsenal, NJ 07806-5000	1	Commander US Army Missile Command ATTN: AMSMI-AS Redstone Arsenal, AL 35898-5000
1	Commander Benet Weapons Laboratory Armament R&D Center US Army AMCCOM ATTN: SMCAR-LCB-TL Watervliet, NY 12189-4050	1	Commander US Army Laboratory Command ATTN: AMSLC-TD Adelphi, MD 20783-1145
1	Commander US Army Armament, Munitions and Chemical Command ATTN: SMCAR-ESP-L Rock Island, IL 61299-7300		

## DISTRIBUTION LIST

<u>No.</u> <u>Copies</u>	<u>Organization</u>	<u>No.</u> <u>Copies</u>	<u>Organization</u>
1	<b>Commander</b> US Army Tank Automotive Command ATTN: AMSTA-DI Warren, MI 48090-5000	5	<b>Director</b> National Aeronautics and Space Administration Ames Research Center ATTN: MS-227-8, L. Schiff MS-258-1, T. Holst MS-258-1, J. Steger MS-258-1, D. Chaussee MS-258-1, M. Rai Moffett Field, CA 94035
1	<b>Director</b> US Army TRADOC Analysis Center ATTN: ATAA-SL White Sands Missile Range, NM 88002-5502	5	<b>Commander</b> US Army ARDEC ATTN: SMCAR-TSS SMCAR-LCA-F J. Grau R. Kline S. Kahn H. Hudgins Picatinny Arsenal, NJ 07806-5001
1	<b>Commandant</b> US Army Infantry School ATTN: ATSH-CD-CSO-OR Fort Benning, GA 31905-5400	1	<b>Air Force Armament Laboratory</b> ATTN: AFATL/DLODL Eglin AFB, FL 32542-5438
1	<b>AFWL/SUL</b> Kirtland AFB, NM 87117-6008	2	<b>United States Military Academy</b> Department of Mechanics ATTN: LTC Andrew L. Dull LTC Thomas Kiehne West Point, NY 10996
2	<b>Commander</b> Naval Surface Weapons Center ATTN: Code R44 (Dr. F. Priolo) Code R44 (Dr. A. Wardlaw) K-24, Building 402-12 White Oak Laboratory Silver Spring, MD 20903-5000	1	<b>Air Force Armament Laboratory</b> ATTN: AFATL/DLODL Eglin AFB, FL 32542-5438
3	<b>Director</b> National Aeronautics and Space Administration Langley Research Center ATTN: Tech Library Mr. P. J. Bobbitt Mr. D. M. Bushnell Langley Station Hampton, VA 23665	2	<b>United States Military Academy</b> Department of Mechanics ATTN: LTC Andrew L. Dull LTC Thomas Kiehne West Point, NY 10996

## DISTRIBUTION LIST

<u>No.</u> <u>Copies</u>	<u>Organization</u>	<u>No.</u> <u>Copies</u>	<u>Organization</u>
1	Massachusetts Institute of Technology ATTN: Tech Library 77 Massachusetts Avenue Cambridge, MA 02139	1	University of Illinois at Urbana Champaign Department of Mechanical and Industrial Engineering Urbana, IL 61801
1	Commander US Naval Surface Weapons Center ATTN: Dr. F. Moore Dahlgren, VA 22448	1	University of Maryland Department of Aerospace Engr. ATTN: Dr. J. D. Anderson, Jr. College Park, MD 20742
1	Air Force Armament Laboratory ATTN: AFATL/FXA (Stephen C. Korn) Eglin AFB, FL 32542-5434	1	University of Notre Dame Department of Aeronautical and Mechanical Engineering ATTN: Prof. T. J. Mueller Notre Dame, IN 46556
1	AEDC Calspan Field Service ATTN: MS 600 (Dr. John Benek) AAFS, TN 37389	1	University of Texas Department of Aerospace Engineering and Engineering Mechanics ATTN: Dr. D. S. Dolling Austin, Texas 78712-1055
1	Virginia Polytechnic Institute & State University ATTN: Dr. Clark H. Lewis Department of Aerospace & Ocean Engineering Blacksburg, VA 24061	1	University of Delaware Department of Mechanical Engineering ATTN: Dr. John Meakin Chairman Newark, DE 19716
1	University of California, Davis Department of Mechanical Engineering ATTN: Prof. H.A. Dwyer Davis, CA 95616	1	University of Florida Department of Engineering Sciences College of Engineering ATTN: Prof. C. C. Hsu Gainesville, FL 32611
1	Pennsylvania State University Department of Aerospace Engineering ATTN: Dr. G. S. Dulikravich University Park, PA 16802		

## DISTRIBUTION LIST

<u>No.</u> <u>Copies</u>	<u>Organization</u>	<u>No.</u> <u>Copies</u>	<u>Organization</u>
2	USAF Wright Aeronautical Laboratories ATTN: AFWAL/FIMG Mr. Norman E. Scaggs Dr. J. Shang WPAFB, OH 45433-6553		<b>Aberdeen Proving Ground</b>  Director, USAMSAA ATTN: AMXSU-D AMXSU-MP, H. Cohen
1	Grumann Aerospace Corporaton Aerophysics Research Department ATTN: Dr. R. E. Melnik Bethpage, NY 11714		Commander, USATECOM ATTN: AMSTE-TO-F  Cdr, CRDC, AMCCOM ATTN: SMCCR-MU SMCCR-RSP-A SMCCR-SPS-IL
1	Advanced Technology Center Arvin/Calspan Aerodynamics Research Department ATTN: Dr. M. S. Holden P. O. Box 400 Buffalo, NY 14225		
2	Director Sandia National Laboratories ATTN: Dr. W. Oberkampf Dr. F. Blottner Division 1636 Albuquerque, NM 87185		

USER EVALUATION SHEET/CHANGE OF ADDRESS

This laboratory undertakes a continuing effort to improve the quality of the reports it publishes. Your comments/answers below will aid us in our efforts.

1. Does this report satisfy a need? (Comment on purpose, related project, or other area of interest for which the report will be used.) \_\_\_\_\_  
\_\_\_\_\_
2. How, specifically, is the report being used? (Information source, design data, procedure, source of ideas, etc.) \_\_\_\_\_  
\_\_\_\_\_
3. Has the information in this report led to any quantitative savings as far as man-hours or dollars saved, operating costs avoided, or efficiencies achieved, etc? If so, please elaborate. \_\_\_\_\_  
\_\_\_\_\_
4. General Comments. What do you think should be changed to improve future reports? (Indicate changes to organization, technical content, format, etc.) \_\_\_\_\_  
\_\_\_\_\_

BRL Report Number \_\_\_\_\_ Division Symbol \_\_\_\_\_

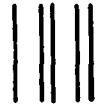
Check here if desire to be removed from distribution list. \_\_\_\_\_

Check here for address change. \_\_\_\_\_

Current address: Organization \_\_\_\_\_  
Address \_\_\_\_\_  
\_\_\_\_\_

-----FOLD AND TAPE CLOSED-----

Director  
U.S. Army Ballistic Research Laboratory  
ATTN: SLCBR-DD-T(NEI)  
Aberdeen Proving Ground, MD 21005-5066



NO POSTAGE  
NECESSARY  
IF MAILED  
IN THE  
UNITED STATES

OFFICIAL BUSINESS  
PENALTY FOR PRIVATE USE \$300

**BUSINESS REPLY LABEL**  
FIRST CLASS PERMIT NO. 12062 WASHINGTON D. C.

POSTAGE WILL BE PAID BY DEPARTMENT OF THE ARMY



Director  
U.S. Army Ballistic Research Laboratory  
ATTN: SLCBR-DD-T(NEI)  
Aberdeen Proving Ground, MD 21005-9989